Ultraviolet-photoluminescence and trace element analyses in Ga-rich sphalerite from the Djebel Gustar Zn-Pb deposit, Algeria

Aleš Šoster, Viktor Bertrandsson Erlandsson, Miloš Velojić, Phillip Gopon

Дигитални репозиторијум Рударско-геолошког факултета Универзитета у Београду

[ДР РГФ]

Ultraviolet-photoluminescence and trace element analyses in Ga-rich sphalerite from the Djebel Gustar Zn-Pb deposit, Algeria

Aleš Šoster [a,*], Viktor Bertrandsson Erlandsson [b], Miloš Velojić [c], Phillip Gopon [b]

[a] University of Ljubljana, Faculty of Natural Sciences and Engineering, Aškerčeva c. 12, SI-1000 Ljubljana, Slovenia
[b] Montanuniversität Leoben, Department of Applied Geosciences and Geophysics, Peter Tunner Straße 5, AT-8700 Leoben, Austria
[c] University of Belgrade, Faculty of Mining and Geology, Djušina 7, RS-10000 Belgrade, Serbia

ARTICLE INFO

ABSTRACT

The Djebel Gustar Zn-Pb deposit in northeastern Algeria is one of many carbonate-hosted base metal deposits in the Atlas metallogenic province of North Africa. The sphalerite in this deposit occurs in five distinct types that differ in texture, mineral assemblage, chemical composition, and UV photoluminescence signature. Detailed investigation of trace elements by laser ablation inductively coupled plasma mass spectrometry (LA-ICP-MS) showed that the sphalerite is significantly enriched in the critical metal Ga. The trace element concentrations of the different sphalerite types correlated well with their photoluminescence color; with Mn^{2+} (orange-yellow), Cu^+ (green), and Ga^{3+} (red) being the dominant activators. We suggest that the Ga enrichment in the Djebel Gustar deposit is the result of formation conditions that include the mixing of a Cl-rich fluid carrying mainly Zn and Pb with a more reduced and Cl-poor fluid containing considerable organic matter and/or calcite with adsorbed $Ga(OH)_3$. This Ga was subsequently incorporated into sphalerite, rather than forming a stoichiometric Ga phase. Furthermore, our study demonstrates that UV photoluminescence of low Fe sphalerite has the potential to become a simple and affordable tool for preliminary characterization of sphalerite ores in mining and exploration with respect to critical elements such as Ga.

1. Introduction

Gallium is a high-tech critical metal essential in the manufacturing of green energy technologies, semiconductors, and biomedical applications (Höll et al., 2007). However, the relative scarcity of easily mineable Ga, has led to it being included on both the EU and USGS lists of critical raw materials (USGS, 2020; European commission, 2020). This means that its supply has been deemed a high risk, with large potential implications for green energy and defense infrastructure. We geologists have therefore been tasked within finding alternative sources.

Although the abundance of Ga in the Earth's crust exceeds that of easier to find/mine metals such as Cu, Ag, and Zn, it rarely forms stoichiometric Ga phases (Négrel et al., 2018; Yuan et al., 2021) making exploration and extraction problematic. Despite the rarity of Ga rich minerals, it is frequently incorporated as a trace element into other minerals (silicates, oxides and sulfides), replacing mainly for Al, Fe, and Zn (Burton et al., 1959). Low-temperature carbonate-hosted Pb-Zn deposits e.g., Mississippi-Valley type deposits (MVTs), are considered a major source of Ga and Ge where it can be won as a byproduct of Pb-Zn

production (Höll et al., 2007; Liu et al., 2023). In these MVT deposits, Ga primarily occurs incorporated within the ore mineral sphalerite (ZnS; Nassar et al., 2015; Yuan et al., 2021). Sphalerite is an important Zn ore and a common accessory mineral in various ore deposits types (di Benedetto et al., 2005; Cook et al., 2009; Murakami and Ishihara, 2013; Belissont et al., 2014; Wei et al., 2018; Xing et al., 2021). Due to its simple halite-like cubic crystal structure, sphalerite can incorporate a variety of minor and trace elements in solid solution (e.g., Mn, Fe, and Cd). During the mineral extraction and processing, some of these trace elements can be efficiently recovered (Ge, Ga, Ag, In, Cd) while others pose a potential environmental hazard (Hg, As, Sb, Bi, Sn, Cd, Se, Te; Cook et al., 2009; Pfaff et al., 2011).

Not all sphalerites in all ore deposit types, or even all sphalerite generations in a single deposit have the same trace elemental signature, both the harmful as well as the useful ones. It is, therefore, critical to know the concentration and the type of trace metals present, prior to developing a mining or smelting plan. However, the analysis of trace metals is both time consuming and expensive, often requiring laser ablation inductively coupled plasma mass spectrometry (LA-ICP-MS) or

---

electron probe micro analyzer (EPMA) analysis of the sphalerite. What is needed is a fast, cheap, and reproducible method to quickly screen sphalerites for their trace metals.

Photoluminescence is the emission of electromagnetic radiation in the visible light spectrum caused by the excitation and subsequent relaxation of valence electrons. In minerals, photoluminescence can almost always be attributed to effects and defects within the crystal structure. This includes the recombination of electron-hole pairs related to lattice defects and the incorporated of trace elements. These trace elements not only distort the crystal lattice but also alter the charge distribution within the crystal structure (Götze, 2002). Specific trace elements may therefore serve to either increase (termed 'activators') or decrease (termed 'quenchers') the photoluminescence of the minerals and/or the wavelength of electromagnetic radiation that is given off (i.e., changing the luminescence color; Çiftçi, 2009). Activators produce photoluminescence by releasing absorbed energy in the form of photons and quenchers trap absorbed energy, resulting in a non-luminescent response. A third group is known as 'sensitizers' which accumulate energy and transfer it to activators, essentially acting as an enhancer for the activator that is present. Sphalerite is an important phosphor and one of the few sulfides that can produce luminescence when excited by an ultraviolet light source (Çiftçi, 2009; Sotillo et al., 2015; Saleh et al., 2019). In synthetic sphalerite the three most common activators have been shown to be Mn, Cu, and Ag, while group IIIa elements (Al, Ga, In) have been shown to modify the luminescence properties of experimentally grown ZnS (Sotillo et al., 2015).

In this study, we present the trace element concentrations and ultraviolet light (UV)-induced photoluminescence signatures of extremely Ga-rich red sphalerite from the Djebel Gustar deposit, located in the Atlas Mountains of NE Algeria. The Atlas Mountains, spanning from the passive Atlantic continental margin of Morocco to the Tunisian Mediterranean coast are known to host more than a thousand MVT mineralizations (e.g., Bouabdellah and Sangster, 2016; Decrée et al., 2016; Laouar et al., 2016; Omar et al., 2016; Ysbaa et al., 2021). However, despite the large number of deposits there has been surprisingly limited research in this part of the world, with what does exist being limited to petrographic observations and studies of fluid inclusions. There are few, studies of the trace elements associated with the principal ore minerals in these deposits.

The Djebel Gustar deposit is one in a series of low-temperature carbonate-hosted Pb-Zn deposits in the Atlas Mountains, wherein sphalerite is the main ore mineral. We performed detailed petrographic analysis of the sphalerite, measured the trace elemental content of these sphalerites using LA-ICP-MS, and compared this to the UV photoluminescence signature. The aim was to investigate the link between the photoluminescence signature of sphalerite with the trace element geochemistry, and use this information to develop an easy, cheap, and straightforward exploration tool for critical elements in sphalerite.

2. Regional geology

Northern Algeria is dominated by two main mountain belts, the E–W trending Tell Atlas in the north and the NE–SW trending Saharan Atlas in the south, which are separated by the High Plateaus (Fig. 1a). South of the Tell Atlas Mountains is the Saharan Shield, which consists of Precambrian cratons and shields as well as Paleozoic intracratonic basins. The Djebel Gustar Pb-Zn mine is stratigraphically located in the South Setífian platform (Fig. 1b) and is part of the High Plateaus of
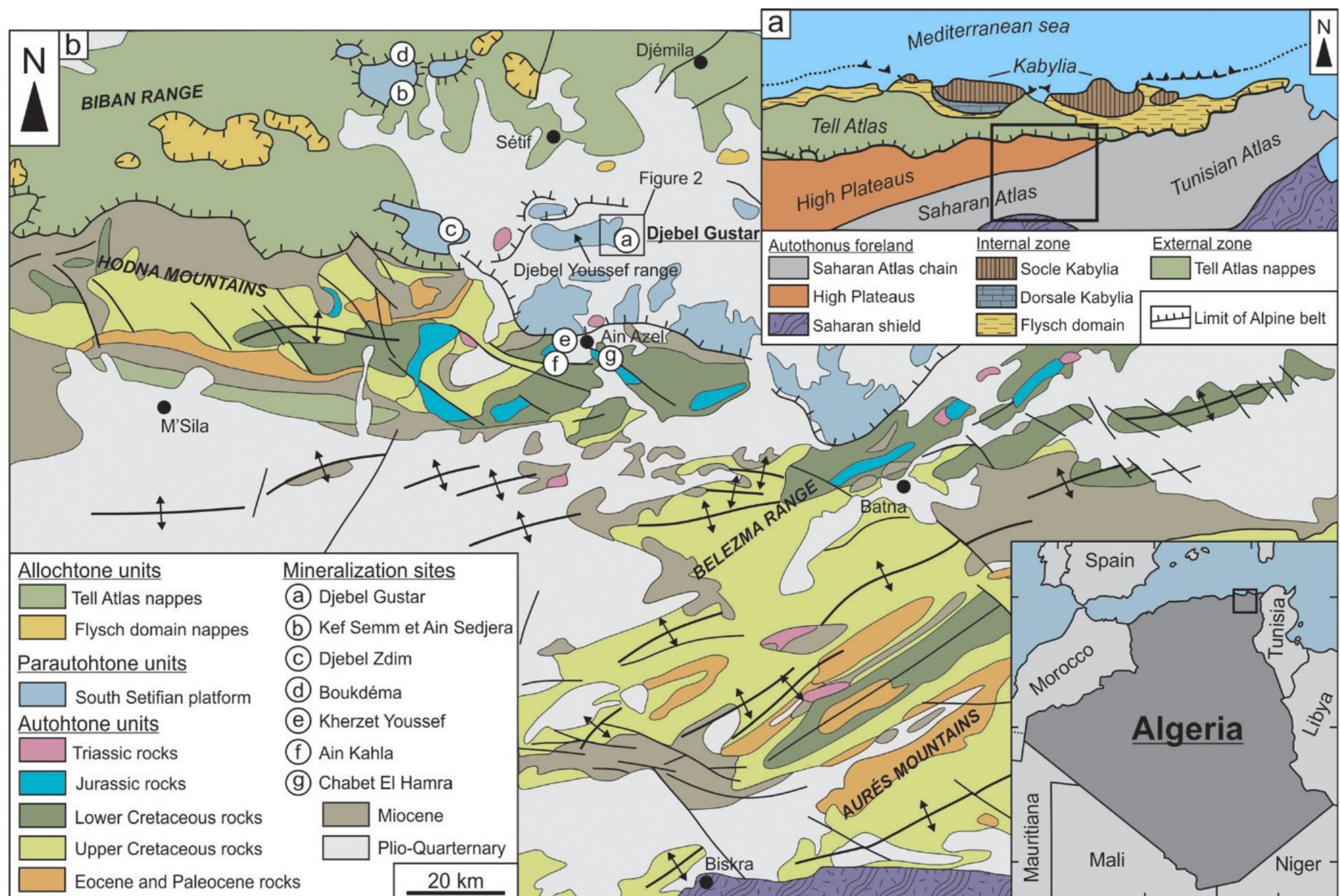

Fig. 1. Regional geologic map depicting the basic structural subdivision of the NE Algeria (a). General geological map of the research area, located between Tell and Saharan Atlas chains (b), indicating the geographic position of the Djebel Gustar mine. Map compiled and modified after Wildi (1983), Boutaleb (2001) and Youcef Brahim et al. (2021).

northeastern Algeria. The South Setifían platform extends along the southern margin of the eastern Algerian Alpine belt, at the convergence front between the allochthonous foreland and the Saharan Atlas Domain (Boutaleb, 2001; Youcef Brahim et al., 2021). In this area, the rock formations are associated with the opening and closing of the Maghreb Basin, which is related to the breakup of Pangea and the convergence of the African and Eurasian plates, which continues to the present day (Martín-Martín et al., 2017; Youcef Brahim et al., 2021). The regional geology is predominantly composed of Jurassic to Cretaceous carbonates, interbedded with fine-grained siliciclastic rocks that reflect the dissection of carbonate platforms due to extensional tectonics associated with the rifting of the southern Tethyan margin (Maghreb Basin). During the Cenozoic, extensional tectonics reversed to compression, resulting in extensive folding and faulting that exposed Mesozoic rocks from the Cenozoic rock cover (Van Hinsbergen et al., 2014; Youcef Brahim et al., 2021).

3. Geology of the Djebel Gustar deposit

The study area is located in the Djebel Gustar mountains, the eastern extension of the Djebel Youssef mountain range (Fig. 1b). Geographically Djebel Gustar is located between the cities Setíf and Ain Azel, 300 km to the southeast of Algiers. The geologic architecture of Djebel Gustar is characterized by a NE–SE oriented anti-form structure, with limbs dipping between 10 and 45° (Boutaleb and Lekbal, 2012; Boutaleb et al., 2016; Lekbal and Boutaleb, 2012; Zahri et al., 2016). The anti-form is composed of Jurassic and Cretaceous carbonates (Youcef Brahim et al., 2021), and is dissected by later normal faults. The Late Jurassic rocks are characterized by *Clypeina jurassica* containing limestone that transition into marl and marly limestone (Fig. 2; J^6). The Cretaceous lithologies are characterized by Barremian massive limestone, dolostone and sandstone (n^4), Aptian yellow marly (n^{5a}) and Aptian-Albian intercalations of limestone, dolomitized limestone, marly limestone, and sandstone (n^6). Surrounding the mountain range are Quaternary slope sediments (Fig. 2; Q_t) (Leikine and Vila, 1977a,b; Boutaleb, 2001).

The Zn-Pb mineralization at Djebel Gustar is hosted in Late Jurassic to Early Cretaceous rocks (Fig. 2). The notable feature of the carbonates at Gustar is an abundance of diagenetic quartz, expressed as small automorphic rods, displaying zonal growth with numerous inclusions of micritic rock and bioclasts (Fig. 3a; Fig. 4a). The mineralization is confined to dolomitized formations and occurs as clusters of irregular lens-shaped stratabound replacement zones and veins, that laterally wedge out and transition to unaltered limestone (Boutaleb, 2001; Lekbal and Boutaleb, 2012). The mineralization occurs in numerous discreet orebodies ranging up to 150 × 20 m in size. The mineral assemblage at Djebel Gustar is relatively simple, consisting predominantly sphalerite, along with galena and minor pyrite. The gangue minerals include quartz, calcite, and dolomite, while supergene zones contain smithsonite, hematite, cerussite and zincite. Detailed description of host-rock and sphalerite is lacking in previous literature and we therefore include a detailed petrographic analysis in this work (see: 'Results' section).

4. Materials and methods

The samples used in this study are historical samples collected by the Yugoslavian geological expedition to Algeria in the 1960s and are part of the sample library of the Faculty of Natural Sciences and Engineering, University of Ljubljana, Slovenia. The material used in this study was collected from the Court, Kes-Kes and Bertiaux orebodies of the Djebel Gustar Zn-Pb mine. A total of 15 representative ore samples from the Djebel Gustar Zn-Pb deposit were selected and petrographically examined by reflected light microscopy and scanning electron microscopy (SEM) to determine their mineralogical composition and the paragenetic relationships between minerals and mineralized structures. Particular attention was given to distinguish different types of sphalerites based on their texture, morphology, and mineral assemblage. The samples analyzed by laser ablation inductively coupled plasma mass spectrometry (LA-ICP-MS) were carefully selected to contain most of the sphalerite types in a clear paragenetic relationship.

Qualitative examination of photoluminescence in sphalerite was performed using a UV-8S/L (Franz Krantz) ultraviolet (UV) lamp containing both 8-watt short ($\lambda = 254$ nm) and long wavelength ($\lambda = 365$ nm) emitters. The sphalerite displayed luminescence only when
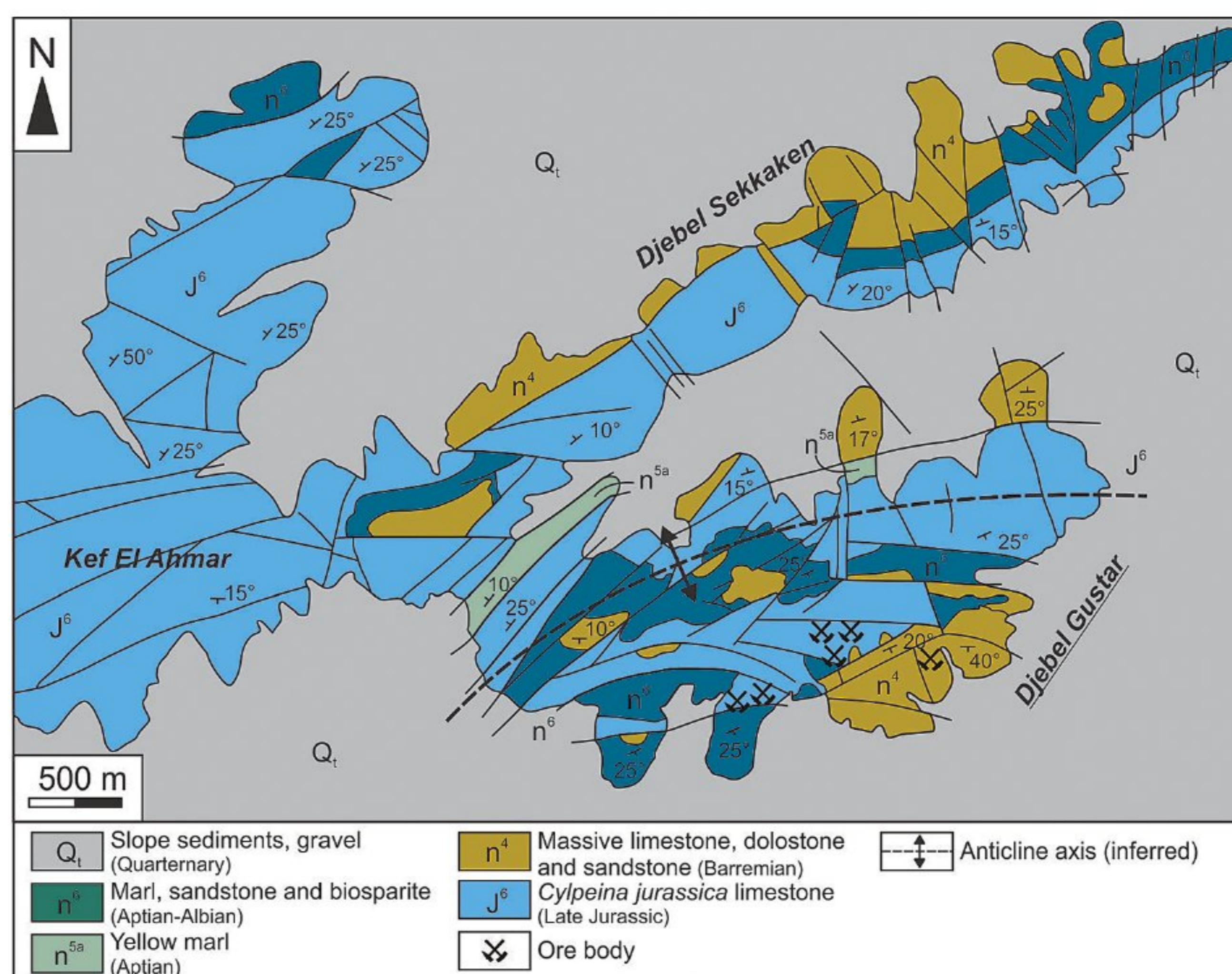

Fig. 2. Geological map of the Djebel Gustar Zn-Pb mine (Leikine and Vila, 1977a,b; Boutaleb, 2001).
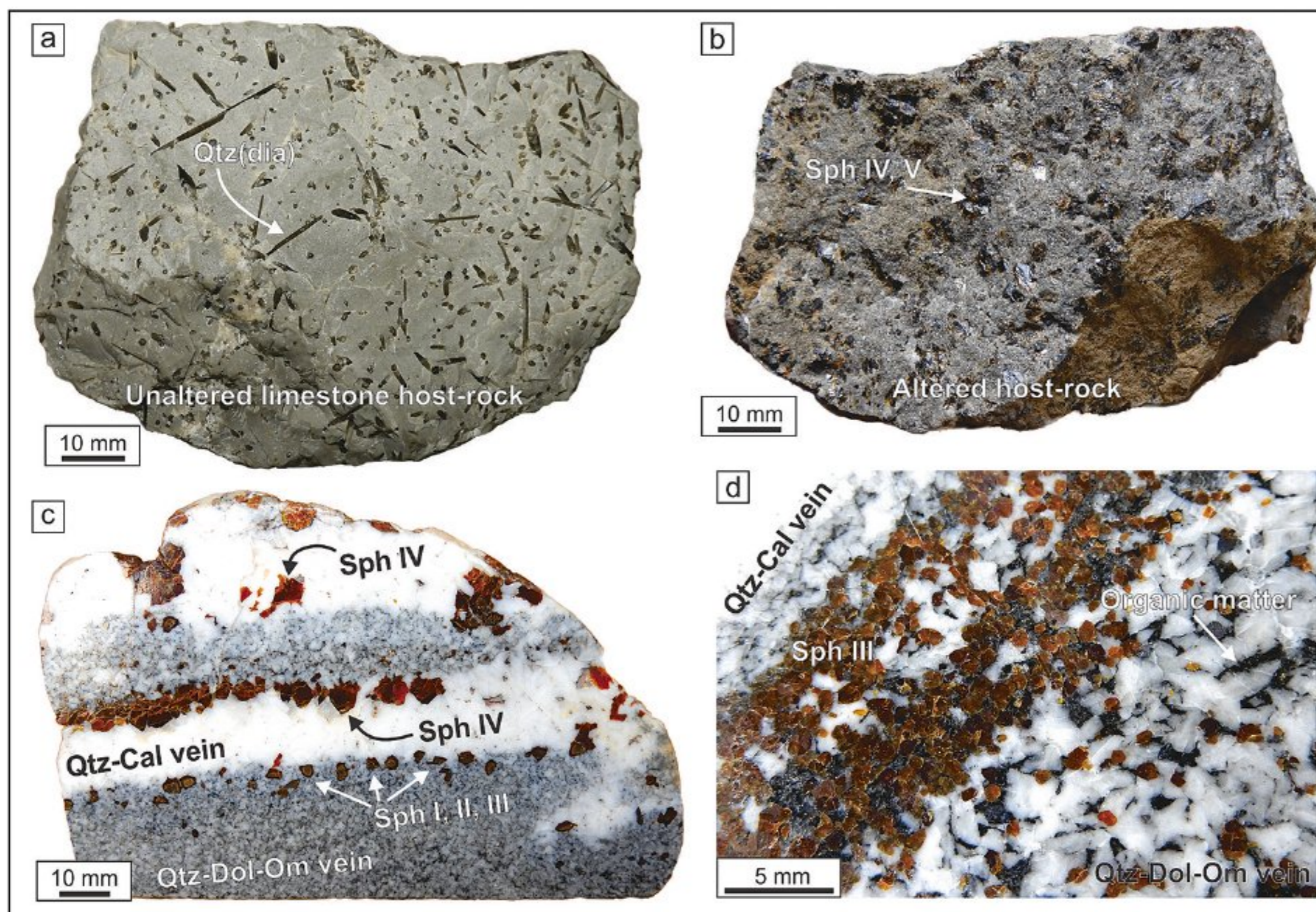
Fig. 3. Representative photographs of host-rock and principal ores from the Djebel Gustar deposit. (a) unaltered host-rock limestone, containing rods of diagenetic quartz; (b) highly altered (dolomitized) host-rock containing crystals of sphalerite; (c) hand-size specimen demonstrating paragenetic relationship between Qtz-Dol-Om and Qtz-Cal veins and corresponding sphalerite types; (d) a detail of Qtz-Dol-Om vein showing distribution of organic matter as infill between grains of dolomite and sphalerite. Key: Qtz – quartz, Qtz(dia) – diagenetic quartz, Sph – sphalerite, Cal – calcite, Dol – dolomite.
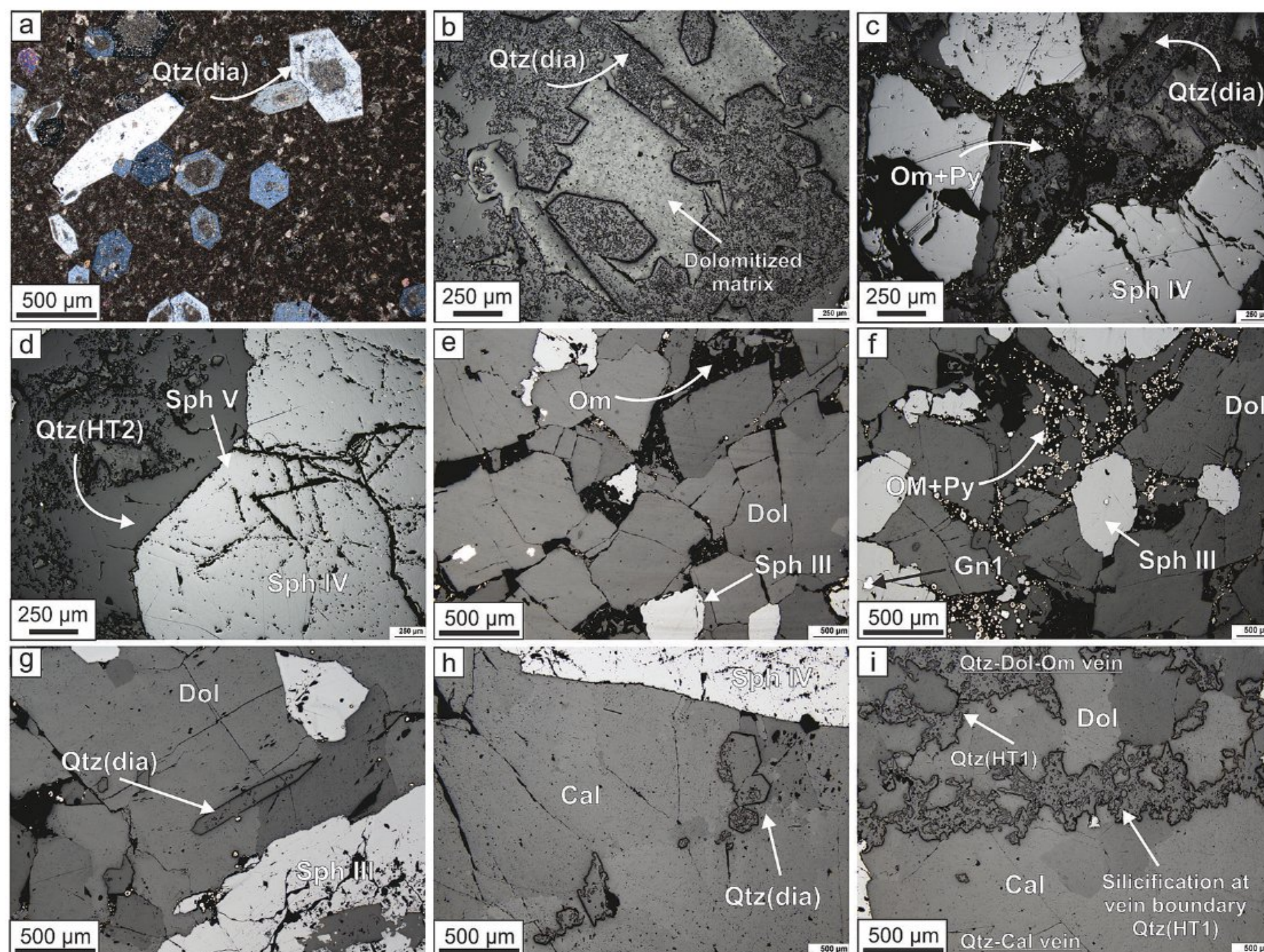

Fig. 4. Representative photomicrographs of principal textures of mineralized rocks from the Djebel Gustar deposit. (a) diagenetic quartz in unaltered host-rock limestone; (b) diagenetic quartz and dolomitic alteration in altered host-rock; (c) mineralization with sphalerite and accumulation of organic matter with pyrite in the porosity of the altered host-rock; (d) hydrothermal quartz surrounding sphalerite crystal in dolomitized host-rock; (e) large grains of euhedral to subhedral dolomite in Qtz-Dol-Om vein; (f) porosity between grains of dolomite filled with organic matter and abundant pyrite; (g) crystal of diagenetic quartz in Qtz-Dol-Om vein; (h) diagenetic quartz crystals in Qtz-Cal vein and (i) silicification at the contact between Qtz-Cal vein (below) and Qtz-Dol-Om vein (above). Key: Qtz(HT) – hydrothermal quartz, Gn – galena, Om – organic matter, Py – pyrite.

illuminated with long wavelength UV light. The UV characterization of sphalerite was performed at the Faculty of Natural Sciences and Engineering, University of Ljubljana.

SEM characterization was performed with the ThermoFisher Scientific Quattro S field emission scanning electron microscope (FEG-SEM) equipped with an Oxford Instruments-UltimMax 65 energy dispersive (EDS) detector. Before analysis, the samples were coated with 20 nm of carbon to ensure the electrical conductivity of the sample. The

instrument was operated at an acceleration voltage of 15 kV and a beam current of 10 nA. The EDS spectra were acquired at 10 mm working distance and 60 s. acquisition time for each measurement. The SEM analysis were performed at the Faculty of Natural Sciences and Engineering, University of Ljubljana.

In situ trace element analyses were carried out with an ESI NWR213 Nd:YAG laser ablation system coupled to an Agilent 8800 triple quadrupole ICP-MS, at the Department of Applied Geosciences and Geophysics, Montanuniversität Leoben, Austria. Masses analyzed were: ^{34}S, ^{51}V, ^{55}Mn, ^{57}Fe, ^{59}Co, ^{60}Ni, ^{63}Cu, ^{65}Cu, ^{67}Zn, ^{71}Ga, ^{72}Ge, ^{73}Ge, ^{74}Ge, ^{75}As, ^{82}Se, ^{95}Mo, ^{107}Ag, ^{111}Cd, ^{115}In, ^{118}Sn, ^{121}Sb, ^{125}Te, ^{197}Au, ^{201}Hg, ^{205}Tl, ^{208}Pb and ^{209}Bi. A spot size of 50 μm was used. Positioning of laser ablation spots were chosen to avoid inclusions, cracks, or other visible impurities. Laser settings where: fluency was set to 5 J/cm^2 and the repetition rate at 10 Hz. Helium was used as the carrier gas at a flow rate of 0.75 L/min. Thirty seconds of pre-ablation background values were collected, followed by 60 s of laser ablation data collection of the minerals. A 30 s wash out delay preceded each analysis to clear out the laser chamber. The matrix-matched sphalerite reference material MUL-ZnS1 (Onuk et al., 2017) was used as external standard with S as the internal standard. To ensure the trace element analyses' quality, the USGS powder pressed polysulfide reference material MASS1 (Wilson et al., 2002) was used as a secondary standard. The MASS1 was used as the external standard for the quantification of Te, Au, Tl and Hg, as the reference material MUL-ZnS-1 is not suitable for these elements. Both reference materials were re-analyzed after 14 unknowns analyzes, for correction of instrumental drift. Data reduction was done using the Iolite 4 software (Paton et al., 2011). Limits of detection were calculated within the Iolite software. Trace element mapping was done using line scans of 25 μm at a scan speed of 10 μm/s. A fluency of 5 J/cm^2 and repetition rate of 10 Hz was used for the mapping, with the same settings used for spot analyses. The maps were generated using the "Imaging" application within the Iolite 4 software. In sphalerite type 'Sph I' only five *in-situ* measurements were performed due to small grain size and numerous inclusions of gangue minerals.

Principal component analysis (PCA) is a widely used convenient multivariate exploratory technique that has the advantage of reducing and transforming a large number of variables to a new, linearly uncorrelated set of variables (Rollinson, 1996). Analyses below the limit of detection (LOD) were replaced by LOD/2 values (Frenzel et al., 2016; Bauer et al., 2019). The imputation was performed on the concentrations of Fe, As, and Sb, while the concentrations of Co, Ni, Se, Tl, Te, Sn, In, and Bi were too low and frequently below detection limit and were not used in the PCA. All concentrations were log-transformed before the PCA to reduce skewness of measured data and achieve near-normal distribution of the dataset.

5. Results

5.1. Host-rock petrography

Mineralization occurs in altered host-rock (Fig. 3b) and in two types of veins: quartz-dolomite-organic matter veins (Fig. 3c, d) and calcite-quartz veins (Fig. 3c). Altered host-rock is characterized by intensive dolomitization, completely overprinting original biomicritic matrix (Fig. 4b). These rocks contain abundant euhedral to subhedral diagenetic quartz crystals. Organic matter, together with pyrite occurs as an infill between quartz and dolomite crystals or in fractures crosscutting the matrix (Fig. 4c). Hydrothermal quartz is present as vein infills surrounding sphalerite crystals (Fig. 4d). Quartz-dolomite-organic matter veins (Qtz-Dol-Om) are characterized by euhedral to subhedral dolomite crystals (Fig. 4e) that measure up to 2 mm and contain small irregular calcite inclusions. The veins contain rods of diagenetic quartz (Fig. 4g). Hydrothermal quartz in these veins follows irregular, dissolution boundaries between dolomite grains, indicating a later stage infilling of open spaces. The organic matter along with pyrite fills in the pores

between dolomite crystals and around galena and sphalerite grains (Fig. 4f). The Qtz-Dol-Om veins are intersected by quartz-calcite (Qtz-Cal) veins (Fig. 3c). Qtz-Cal veins consist mostly of coarse-grained white calcite (up to 10 mm in diameter) and contain minor amounts of diagenetic quartz (Fig. 4h). Diagenetic quartz contains inclusions of pyrite which are otherwise not found in calcite. The contact between the two types of veins is silicified (Fig. 4i).

5.2. Mineral paragenesis

Based on the petrographic relationships between minerals, the mineralization at Djebel Gustar can be divided into four stages (Fig. 5). Stage 1 occurred during diagenesis and is associated with the formation of diagenetic quartz and pyrite. Stage 2 is marked by sulfide mineralization with sphalerite types I and II. The processes involved in their formation are unresolved as initial alteration and structures are overprinted by dolomitization that occurred during Stage 3. Stage 3 is marked by extensive dolomitization and formation of replacement veins (Qtz-Dol-Om veins) and precipitation of sphalerite type III (Sph III). During Stage 3 Sph types I and II were fractured, bleached, corroded, and reworked by hydrothermal fluids. Sph types I and II were also overgrown and cemented by newly precipitated Sph III and the first generation of galena (Gn I), while matrix pores were partially filled by pyrite, organic matter and the first generation of hydrothermal quartz (Qtz(HT1)). The final stage, Stage 4, is characterized by the formation of Qtz-Cal veins (calcitization) and the precipitation of sphalerite types IV and V. Sphalerites are overgrown by a second generation of hydrothermal quartz (Qtz(HT2)) and replaced by a second generation of galena (Gn II).

5.3. Sphalerite types

Based on macroscopic, microscopic, and long-wave UV luminescence observations, five types of sphalerites can be distinguished (Fig. 6):

Sph I is associated with Qtz-Dol-Om veins. It occurs as round aggregates up to 250 μm in diameter, with bands of various shades of white, brown, and yellow (Fig. 7a). The sphalerite aggregates contain abundant inclusions of quartz, and carbonate-phases and small grains of euhedral pyrite (Fig. 7a–c). In general, the aggregates of Sph I have a saccharoidal appearance, and are bleached and corroded. The open spaces between the aggregates of Sph I are open or partially cemented by a later generation of sphalerite (Fig. 7c). The boundaries between Sph I and the cementing sphalerite are silicified (Fig. 7c). Galena is not associated with this sphalerite type. Sph I shows no luminescence under UV light (Fig. 6a).

Sph II strictly occurs in Qtz-Dol-Om veins, forming yellow zones surrounding the sphalerite type Sph I (Fig. 7a, b). Sph II forms rounded, corroded, and bleached aggregates of saccharoidal appearance that often have discontinuous, alternating bands of color zoned white, yellow, and light red sphalerite (Fig. 7d). Common inclusions in Sph II are quartz and carbonate. Silicification and carbonatization is common and may occur at aggregate boundaries or parallel to the alternating bands of color-zoned sphalerite. Sph II is surrounded by sphalerite Sph III (Fig. 7a, f). The contact with Sph III is silicified and porous. The Sph II shows orange-yellow luminescence under UV light (Fig. 6b).

Sph III is only found in Qtz-Dol-Om veins. Sph III is dark red to orange and occurs as euhedral to subhedral crystals with strong red internal reflections. In Qtz-Dol-Om veins Sph III occurs either independently as the only Sph type or in assemblage with sphalerite types Sph I and Sph II (Fig. 7a, b, f). This type of sphalerite contains inclusions of pyrite, galena, and less commonly quartz and carbonate gangue (Fig. 7e). Galena (Gn1) is present at the outer edges, or it intersects the grains of Sph III. The contact may be straight or serrated indicating the replacement of Sph III by Gn1. In transmitted light the Sph III displays irregular color zoning that appear to represent disrupted growth zones of the crystals (Fig. 7g). Sph III shows dim red luminescence under UV light

	Diagenesis	Epigenesis		
	Stage 1	Stage 2	Stage 3	Stage 4
Quartz	············· Qtz(dia)		······· Qtz(HT1)	······· Qtz(HT2)
Pyrite	··········		······	
Dolomite		Dolomitization (?) ·················	Dolomitization Qtz-Dol-Om veins	Calcitization Qtz-Cal veins
Calcite				·················
Sphalerite		·····Sph I···· ····Sph II····	····Sph III····	Sph IV Sph V ··············
Galena			Gn I ······	Gn II ······

Fig. 5. Paragenetic sequence of mineral deposition in Djebel Gustar deposit.
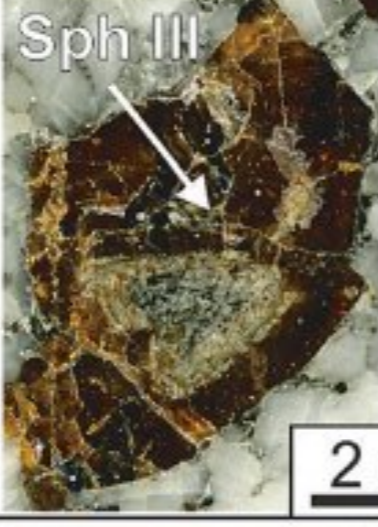
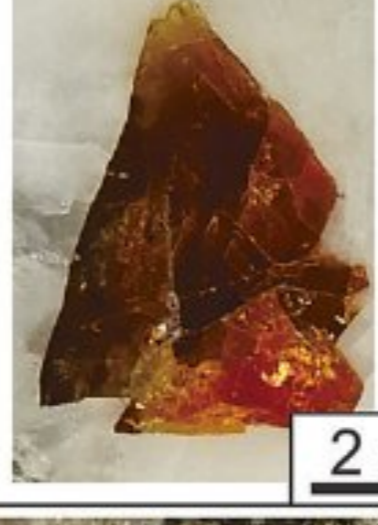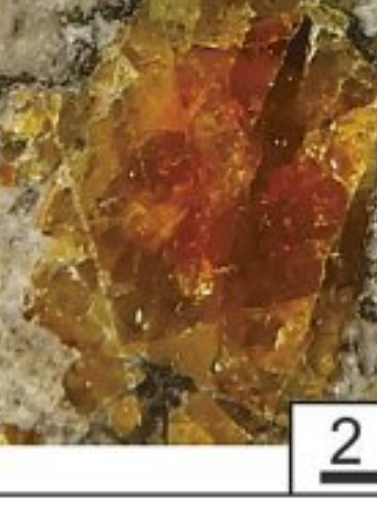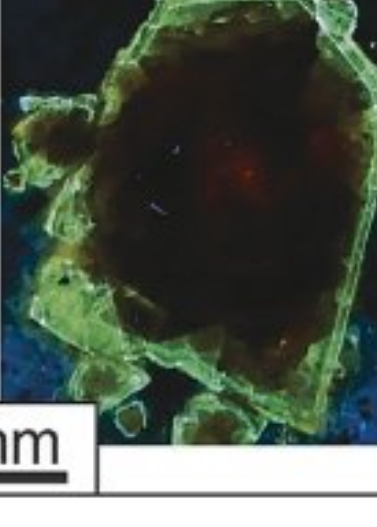| Sphalerite type	Visible light	Ultraviolet luminescence	Texture	Mineral assoc.	Crystal size
Sph I			Anhedral rounded aggregates with many inclusions of gangue minerals and Py. Sphalerite has a saccharoidal and bleached appearance and occurs in brown, white, and yellow varieties. Occurs encompased by bands of Sph II and overgrown by Sph III. UV luminescence: unreactive	Qtz-Dol-Om veins Sph II + Sph III + Dol + Qtz(dia) + Py	up to 250 μm
Sph II			Anhedral, yellow zones surrounding Sph I. Bleached, corroded and saccharoidal in apperanece. Displays discountinous alternating bands of white, yellow and light red sphalerite. Inclusions of Qtz(dia) and dolomite. Overgrown by Sph III. UV luminescence: orange-yellow	Qtz-Dol-Om veins Sph I + Sph III + Dol + Qtz(dia) + Py	up to 500 μm
Sph III			Euhedral to subhedral grains of red or orange-red sphalerite. Occurs alone or in assemblage with Sph I and II. Inclusions are pyrite, less commonly dolomite and Qtz(dia). Replaced and/or intersected by Gn1. Displays disrupted color zoning. UV luminescence: weak red or absent	Qtz-Dol-Om veins Sph I ± Sph III ± Dol + Qtz(dia) + Gn1 + Py + Om + Qtz(HT1)	1 - 5 mm
Sph IV			Euhedral to subhedral grains of red or orange-red sphalerite. Displays oscilatory color zoning. Contains minor inclusions of Py and Gn2. UV luminescence: Dark to bright red	Qtz-Cal veins Cal + Qtz(dia) ± Py Altered host-rock Dol + Qtz(HT2) + Om + Gn2 ± Sph V	5 - 20 mm
Sph V			Honey yellow, slightly bleached and corroded sphalerite, occuring as thin bands surrounding Sph IV. Outter rim surrounded by Qtz(HT2). UV luminescence: bright green	Altered host-rock Sph IV + Dol + Qtz + Om + Py + Gn2 + Qtz(HT2)	up to 1 mm

Fig. 6. Summarization of properties of sphalerite type from the Djebel Gustar deposit.

(Fig. 6c).

Sph IV is red colored and occurs within Cal-Qtz veins and in strongly altered host-rock. Sph IV grains, associated with altered host-rock, are euhedral to subhedral and are up to 20 mm in diameter. This type of sphalerite contains minor inclusions of galena, pyrite, quartz, and carbonate. Sph IV occurs in altered host-rock surrounded by thin zones of Sph V. In the Qtz-Cal veins, Sph IV occurs as crystals growing perpendicular to the vein wall at the contact between Qtz-Dol-Om veins (Fig. 7h). When illuminated with UV light, this sphalerite type produces a dark to bright red luminescence that follows the primary growth zones of the crystal, possibly indicating alternating compositional zoning

(Fig. 6d).

Sph V is associated with the sphalerite type Sph IV occurring in altered host-rock. Sph V occurs as thin bands surrounding Sph IV (Fig. 7i). Sph V has a green to honey yellow color and appears slightly bleached and discolored under reflected light compared to Sph IV. No porosity or inclusions were observed. The outer rim of Sph V is surrounded by a layer of inclusion-free hydrothermal quartz along with minor galena (Gn2) that forms serrated embayments suggesting replacement of sphalerite. This type of sphalerite emits bright green luminescence and phosphorescence when illuminated with UV light (Fig. 6e).
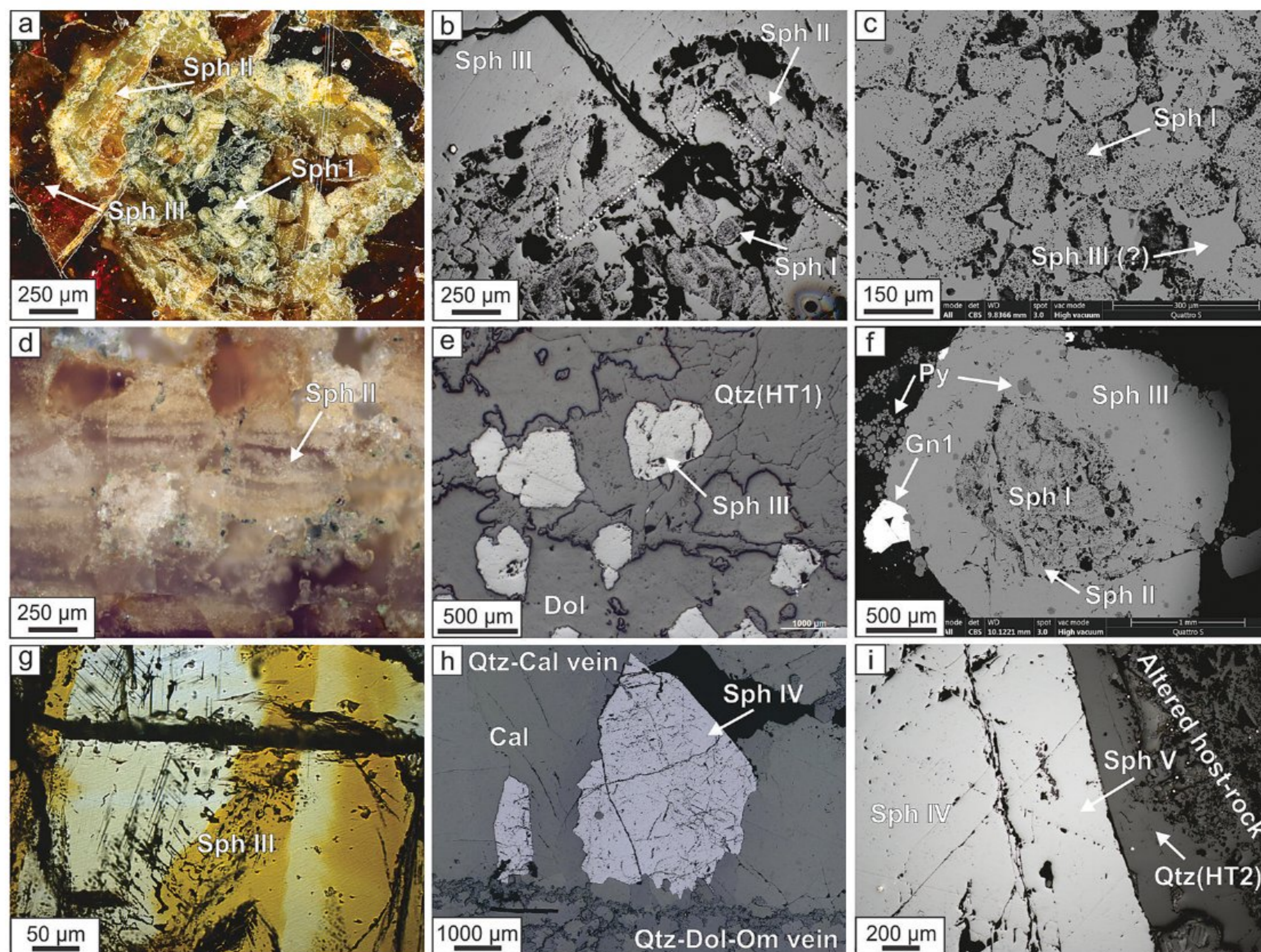
Fig. 7. Microstructural characteristics of the sphalerite types from the Djebel Gustar deposits. (a) Aggregate composed of bleached and corroded Sph I and II, overgrown by Sph III in Qtz-Dol-Om vein, (b) bands of Sph II, enveloping rounded aggregates of Sph I, (c) rounded grains of Sph I, containing numerous inclusions pf gangue dolomite and quartz, (d) discontinuous alternating banding characteristic of Sph II, (e) subhedral crystals of Sph III interconnected by hydrothermal quartz, (f) SEM-BEI image of Sph I, II and III aggregate terminated by first generation galena (Gn1), (g) color zoning in a crystal of Sph III, (h) large crystal of Sph IV in Qtz-Cal vein and (i) crystal of Sph IV, surrounded by band of Sph V and second generation hydrothermal quartz in altered host-rock.

Table 1
LA-ICP-MS results for the different sphalerite types from the Djebel Gustar deposit. All data given in mg kg^{-1}.

		Mn	Fe	Cu	Ga	Ge	As	Ag	Cd	Sb	Hg	Pb
Sph I	Min.	1.97	488	468	133	121	0.48	0.97	1480	0.08	139	27.02
(n = 5)	Mean	5.67	1780	888	168	322	3.68	3.23	1747	2.65	192	37.47
	Median	5.88	2041	768	168	296	2.80	2.61	1634	2.20	171	31.21
	Max.	9.63	2185	1635	212	673	11.47	7.25	2203	5.80	283	54.17
	S.D.	3.04	725	481	31.4	224	4.51	2.41	286	2.70	56.01	14.62
Sph II	Min.	2.05	10.63	48.9	7.90	3.83	0.40	0.48	1473	0.27	131	2.62
(n = 14)	Mean	26.24	145	288	218	29.8	6.93	1.61	1941	4.14	251	16.88
	Median	33.80	55.59	257	198	22.57	4.20	1.24	1932	1.04	230	9.66
	Max.	53.34	533	555	565	80.86	28.60	6.24	2353	35.65	494	61.82
	S.D.	17.27	187	165	163	24.85	8.32	1.57	282.3	9.96	83.24	20.88
Sph III	Min.	4.35	135	69.6	4.13	25.8	0.62	0.13	2303	0.15	96.5	1.08
(n = 17)	Mean	6.78	353	1145	257	325	70.82	2.81	3021	84.53	233	25.25
	Median	6.55	277	1104	210	335	37.32	2.38	2827	42.54	262	16.47
	Max.	8.95	897	2335	930	689	251	8.54	4026	297	456	71.97
	S.D.	1.21	196	725	254	203	78.33	2.37	517	92.46	106	25.09
Sph IV	Min.	5.17	13.79	435	425	40.7	0.84	0.34	2373	0.30	306	0.36
(n = 17)	Mean	9.11	491	1609	1472	209	8.80	1.68	2639	11.23	468	5.37
	Median	8.18	84.3	1704	1731	167	5.23	0.87	2507	7.28	439	3.01
	Max.	14.63	7011	2157	2108	407	36.80	8.71	3337	45.59	611	24.82
	S.D.	3.39	1680	501	568	126	10.06	2.18	280	13.11	99.8	6.35
Sph V	Min.	15.51	13.59	269	298	1.11	0.43	0.30	2262	0.01	660	0.40
(n = 10)	Mean	20.28	17.02	494	588	5.57	0.86	0.38	2587	0.12	827	0.57
	Median	21.35	17.21	526	610	3.53	0.72	0.35	2417	0.10	849	0.58
	Max.	24.52	21.48	678	800	16.57	1.72	0.58	3039	0.40	992	0.81
	S.D.	3.01	2.77	122	157	5.05	0.38	0.10	329.3	0.10	138	0.12

5.4. Sphalerite mineral chemistry

A total of 63 LA-ICP-MS *in-situ* analyses were carried out on the 5 different types of sphalerite from the Djebel Gustar deposit. The statistical parameters of each sphalerite type are listed in Table 1 and shown graphically in Fig. 8 as box-and-whiskers plots. A notable feature of the Djebel Gustar data set is the high variance in trace element concentrations, with standard deviations in some cases exceeding the mean values of a given element (Table 1). Although sub-microscopic inclusions where not present at the surface of the analyzed ablation spots, this does not preclude their existence below the sample surface, which could affect statistical data distribution. Significant variations in the time-resolved profiles are generally interpreted as inclusions, and where thus removed from the analysis to attain representative data for the sphalerite itself. Representative time-resolved profiles for each sphalerite type are given in Appendix 2.

In the crystals of Sph I, only five laser ablation points were obtained due to numerous small inclusions of gangue minerals, making it difficult to attain representative measurements of the material. The most notable feature of Sph I is its high Fe concentrations (488–2185 mg kg^{-1}; median: 2042 mg kg^{-1}) compared to all other sphalerite types (Table 1, Fig. 8). Sph II is highly depleted in trace elements but has elevated concentrations of Mn (2–53 mg kg^{-1}; median: 33.80 mg kg^{-1}), compared to the rest of the data set. Sphalerite type III is rich in trace elements and is characterized by the highest concentrations of Ge (25.8–893 mg kg^{-1}; median: 335 mg kg^{-1}) as well as Cd, As, Sb, and Pb (Table 1, Fig. 8). In contrast, the most notable feature of Sph IV is that it is significantly enriched in Ga (425–2108 mg kg^{-1}; median: 1731 mg kg^{-1}) and relatively poor in Ge (40–407 mg kg^{-1}; median: 167 mg kg^{-1}). In addition, Sph IV contains high concentrations of Cu (435–2157 mg kg^{-1}; median: 1704 mg kg^{-1}), Cd (2373–3337 mg kg^{-1}; median: 2507 mg kg^{-1}), and relatively high concentrations of Hg (306–611 mg kg^{-1}; median: 439 mg kg^{-1}). Sphalerite V is characterized by highest concentrations of Hg (660–992 mg kg^{-1}; median: 849 mg kg^{-1}), compared to the entire data set. Sphalerite V is also rich in Ga (median: 610 mg kg^{-1}) and poor in Ge (median: 3.35 mg kg^{-1}), and contains elevated concentrations of Cu, and Cd and only small amounts of the other trace elements.
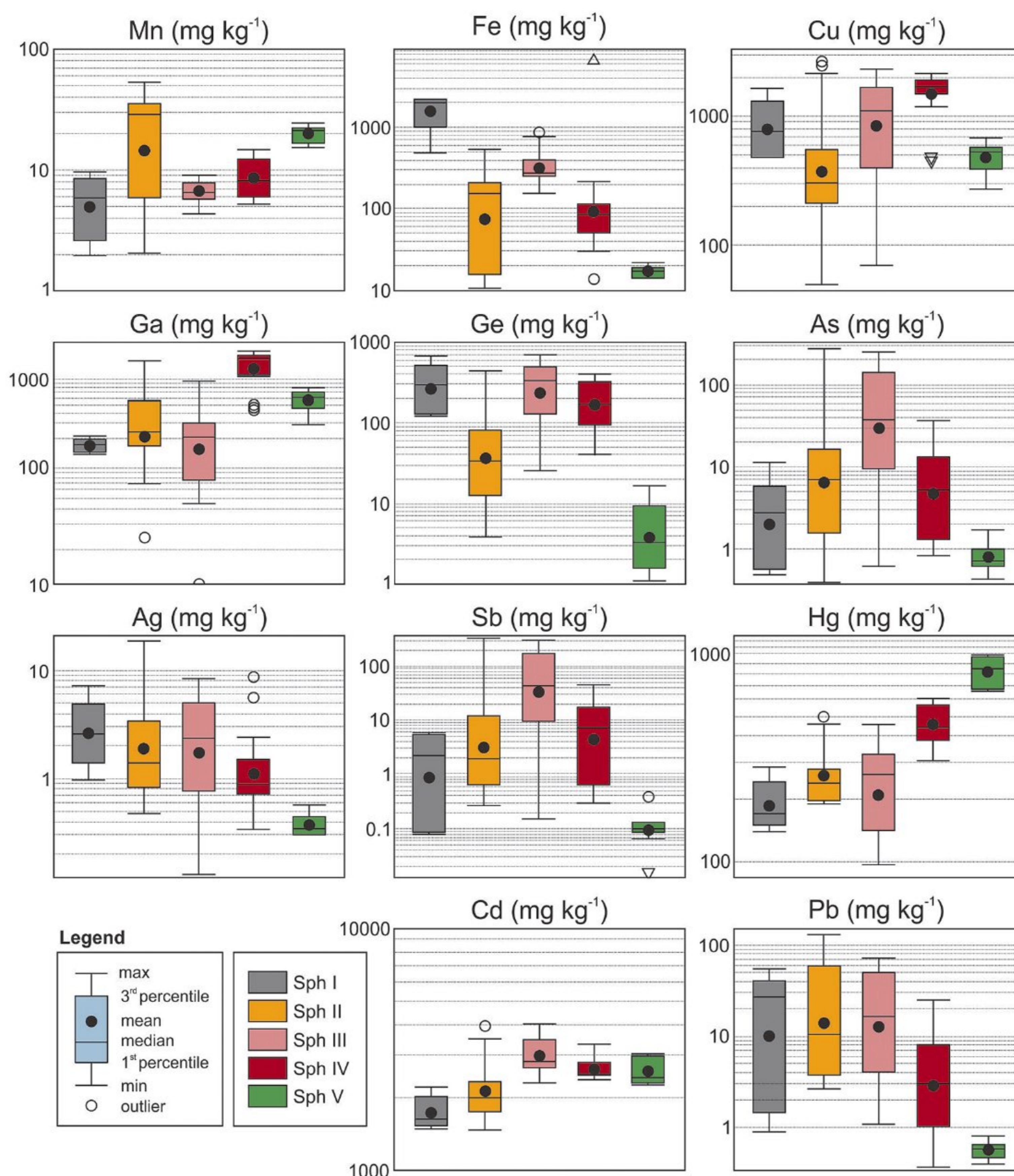

Fig. 8. Box-and-whisker plots depicting minor and trace element composition of studied sphalerite types from the Djebel Gustar deposit. All data given in mg kg^{-1}.

LA-ICP-MS mapping was performed on a euhedral sphalerite crystal that contain the boundary between sphalerite types IV and V (Fig. 6e & 6i). Such maps can be effectively used to highlight the differences in trace element incorporation during crystal growth. The elemental maps (Fig. 9) show an oscillatory zoned distribution of trace elements, particularly Cu, Ga, and Ge, whereas the zonation with respect to Hg and Mn is visible but less pronounced. It is worth noting that even within one type of sphalerite there is compositional variation and zonation (e.g., Cu, Ga, and Ge), which explains variations within the dataset for each sphalerite type. A notable feature of the maps is the positive correlation between Cu and Ga and their concurrent negative correlation with Ge in the crystal core representing the Sph IV. The rims of the crystal, belonging to Sph V, are characterized by an enrichment of Hg (827–992 mg kg^{-1}) and Mn (15–24 mg kg^{-1}) and a decrease in Ge concentration. Other elements (e.g., Ag, Fe, Pb, Sb) are present in low concentrations and appear to be uniformly distributed in the sphalerite and only enriched in the gangue minerals surrounding the crystal and within fractures (Fig. 9).

The PCA results of the Djebel Gustar sphalerites are summarized in Fig. 10. Principal components (PC) 1 and 2 together explain 66 % of the total variance. The binary plots of the remaining nine PCs are not shown in the figure because they do not provide any additional information. The binary PC1 vs. PC2 diagrams (Fig. 10c, d) clearly demonstrate the differences between the sphalerite types studied. PC1 accounts for 46 % of the explained variance and is occupied by Ge, Fe, Ag, As, Sb, and Pb. PC2, accounting for 20 % of the explained variance, is loaded with Hg, Ga, Cu, Mn, and Cd. Cd does not appear to be an important discriminating element since it is omnipresent in high concentrations in all analyzed sphalerite types, as demonstrated by the LA-ICP-MS trace element map (Fig. 9). PC2 is divided into two subgroups, one of which consists of Hg and Mn belonging to Sph V samples, whereas the second group, represented by Ga and Cu, corresponds to Sph IV samples (Fig. 10d). The PC1 loaded with measurements corresponding to sphalerite varieties I and III.
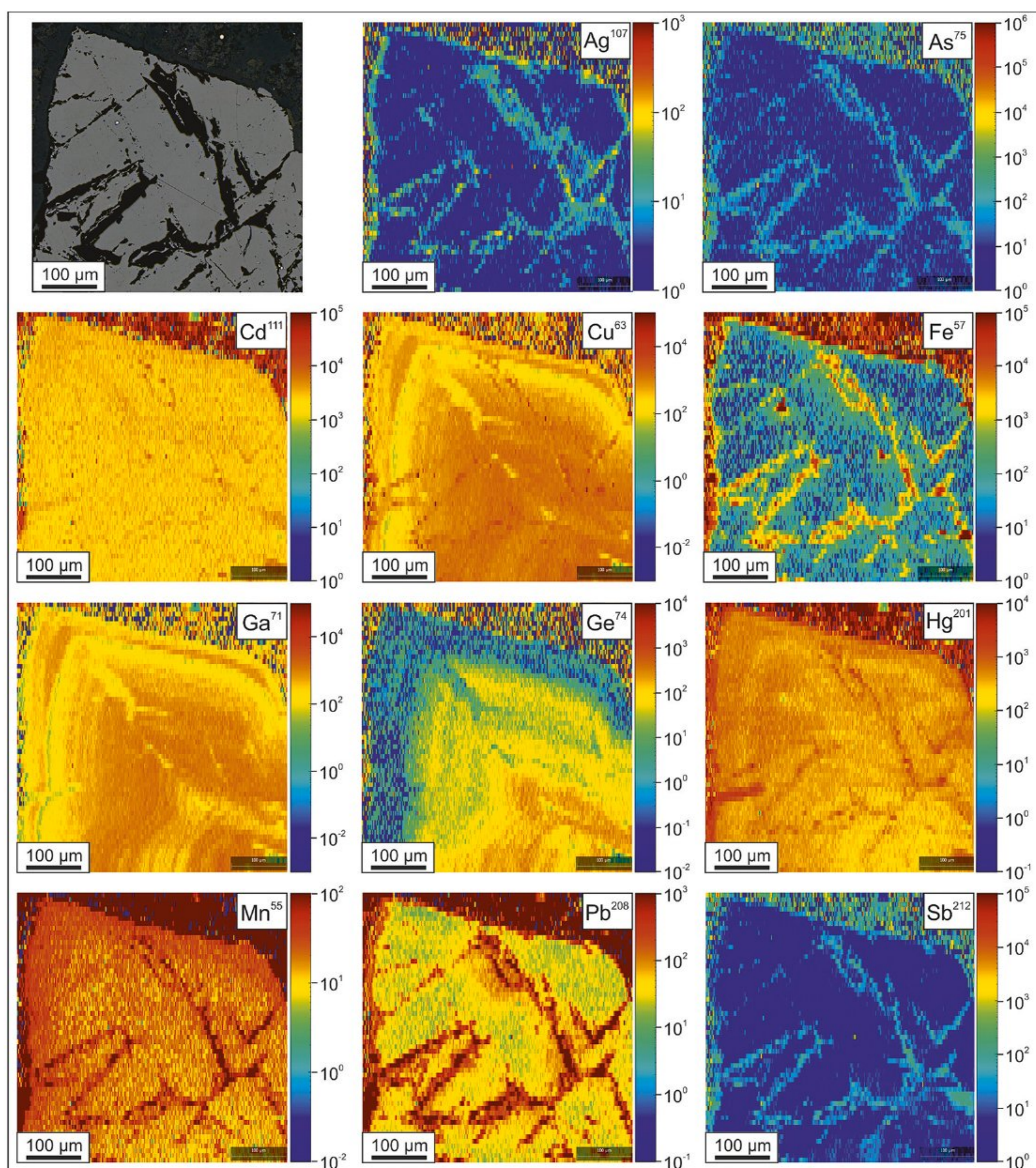

Fig. 9. LA-ICP-MS elemental maps of Ag, As, Cd, Cu, Fe, Ga, Ge, Hg, Mn, Pb, and Sb of a euhedral sphalerite crystal of Sph IV, surrounded by a rim of Sph V, from an altered host-rock sample. The maps of Cu, Ga, Ge, Hg and Mn clearly illustrate the chemical zoning in sphalerite crystal along successively precipitated growth zones. Top left image is a reflected light photomicrograph of the mapped sphalerite crystal. Elements are presented in alphabetical order. The color-scale for all images is in mg kg^{-1}.
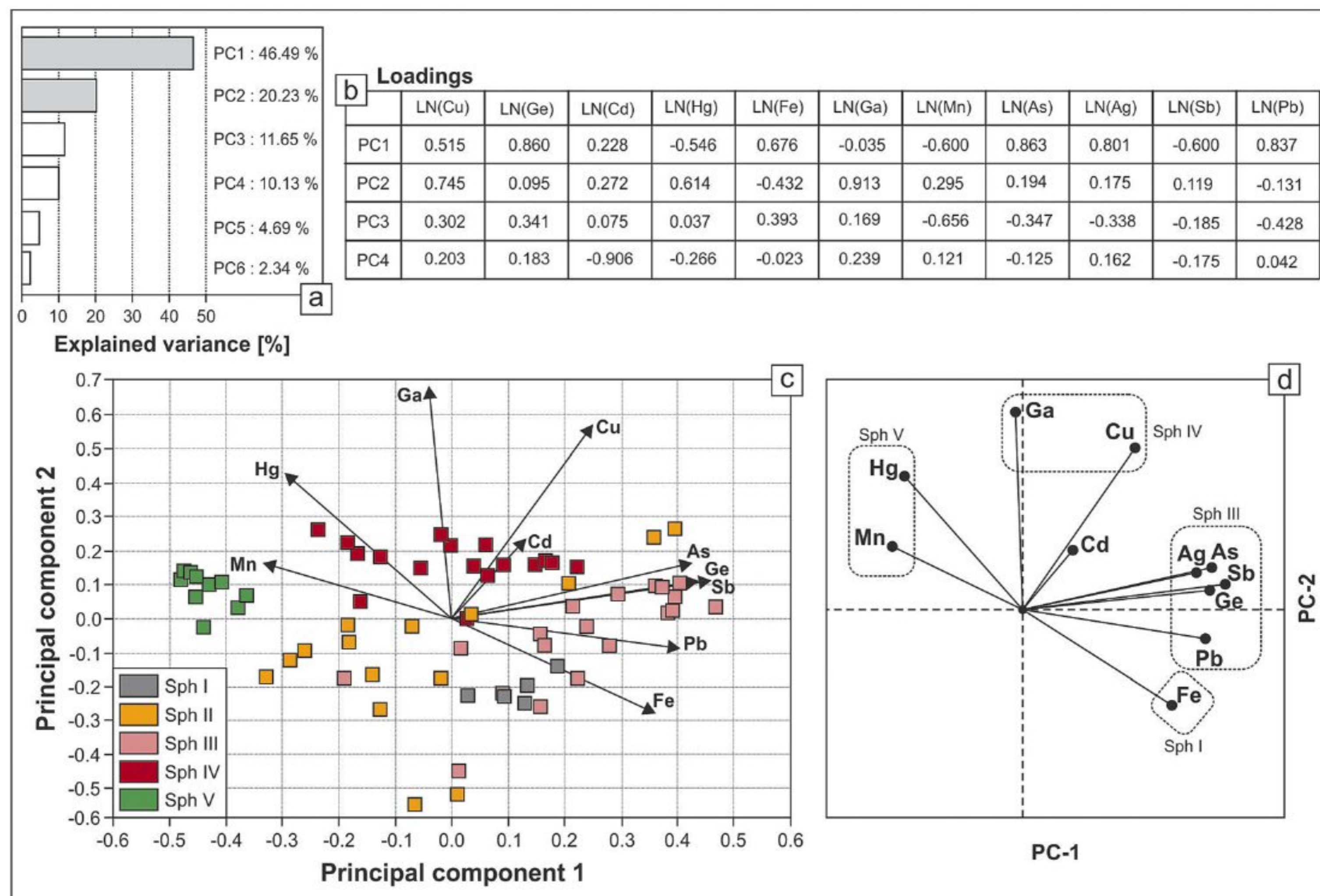
Fig. 10. Principal component analysis of log-transformed trace element concentrations of the Djebel Gustar sphalerite types. The figure shows eigenvalues (explained variability) (Fig. 7a) and data of the loadings (eigenvector coefficients) (Fig. 7b) of the different principal components (Fig. 7c), covariance diagram and a simplified circular diagram (Fig. 7d), corresponding to the covariance diagram. The covariance diagram illustrates the differences between the five sphalerite populations. The angle between the two vectors in diagrams (c) and (d) is linked to the covariance between two chemical elements. Angle close to 90° means that the elements are not correlated, while an angle close to 0° or 180° suggests that two elements are positively or negatively correlated, respectively.

6. Discussion

6.1. Trace element variation and implication

The sphalerite types crystallized during the three sphalerite-forming mineralization stages have different chemical signatures. Several trends are observed between the three mineralization stages: an increase in the mean concentrations of Mn, Ga, and Hg and a decrease in Fe, Ge, Ag, and Pb in sphalerite types I–V (Fig. 8). Some of these trends could have genetic implications.

Stage 2, responsible for the formation of sphalerite types I and II, and

shows an anticorrelation in Fe and Mn concentrations, with Sph I elevated in Fe and Sph II significantly enriched in Mn and with significantly lower Fe concentrations. Sphalerite that precipitated during the later stages (3–4) shows a gradual increase in Mn and a decrease in Fe concentrations (Fig. 8; Fig. 11a). Manganese and iron have been demonstrated to correlate with formation temperature, with increased concentrations of Mn and Fe in sphalerite correlating with higher formation temperatures (Frenzel et al., 2016). However, the sphalerite from Djebel Gustar shows an overall negative correlation trend between Mn and Fe among the five sphalerite generations (Fig. 10c, Fig. 11a), suggesting that temperature is not the primary reason for the Mn
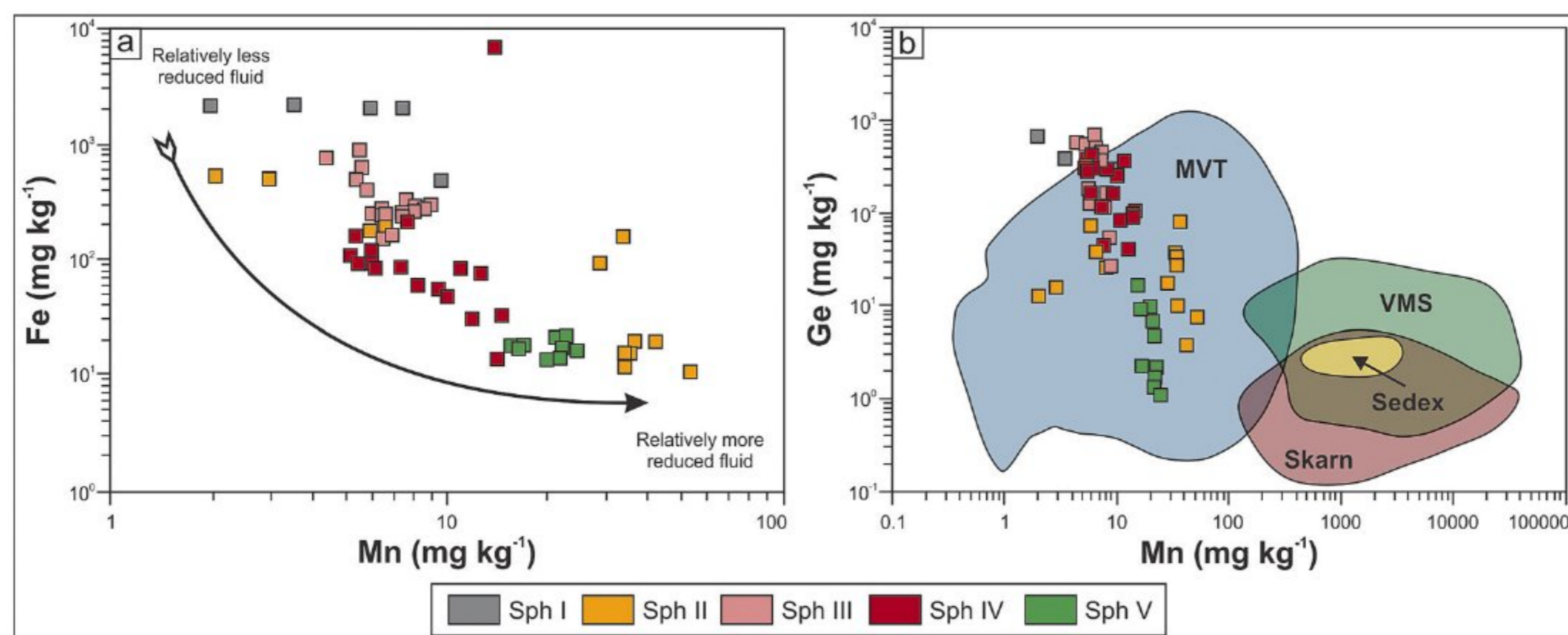

Fig. 11. (a) The Fe vs. Mn diagram shows a pronounced anti-correlation of elements between sphalerite generations, indicating an increase in the reducing ability of the hydrothermal fluid during precipitation of the different sphalerite types. (b) The comparative plot of Ge vs. Mn in sphalerite from the major deposit types. The data show that sphalerite from Djebel Gustar well coincides with sphalerites from MVT deposits. Sphalerite deposit affinity types adopted from Liu et al. (2022). Data collected from: Cook et al. (2009), Ye et al. (2011), Belissont et al. (2014), Bonnet et al., 2016; George et al. (2015, 2016), Yuan et al. (2018), Zhuang et al. (2019), Lee et al. (2019); Li et al. (2019), Cugerone et al. (2021), Cave et al. (2022), Luo et al. (2022).

increase from sphalerite generations I–V. Alternatively, Mn in sphalerite has been proposed to be strongly influenced by the redox state of the ore-forming fluids, with higher Mn in sphalerite associated with more reduced fluid conditions (Kelley et al., 2004; Hu et al., 2021; Liu et al., 2022). The reasoning behind this mechanism is that under reduced conditions Mn is unable to precipitate out as Mn-oxides and thus has to incorporate into the sphalerite crystal structure as MnS (Vaughan and Craig, 1997; Kelley et al., 2004). Therefore, the increasing Mn content in the context of Stage 2 might indicate that Sph I crystallized from a more oxidized fluid comparing to Sph II. A similar trend in increasing Mn concentrations can be observed as a gradual negative linear trend of sphalerite deposited in Stages 3 and 4, suggesting that the redox conditions were increasingly more reduced in each subsequent stage (Fig. 11a). This is further supported by the presence of organic material accumulations associated with altered host-rock mineralization (Sph IV and V) and Qtz-Dol-Om veins (Sph III), indicating that the organic material was introduced primarily after sedimentation by a separate hydrothermal fluid (i.e., during burial and diagenesis or during hydrothermal Pb-Zn mineralization) as such accumulations are not present in unaltered limestone.

Mercury correlates positively with Mn (Fig. 12c) in sphalerite types IV and V. Studies of active hydrothermal fluids and gases have shown that Hg tends to be elevated in Cl-poor and low pH fluids (Roberts et al., 2021). This supports the idea that fluid mixing is responsible for the increasing Mn (and Hg) content in sphalerite, since Pb and Zn are preferentially transported as Cl-complexes in low-temperature hydrothermal fluids and precipitate when ore fluids interact with reduced sulfur (e.g., fluid mixing; Zhong et al. 2015).

The Ge vs. Mn diagram (Fig. 11b) summarizes the chemical composition of sphalerite from the major sphalerite-bearing deposit types. The sphalerites from the Djebel Gustar deposit fit well within the affinity field of other MVT deposit types worldwide. The exception is the significant enrichment of the sphalerite types IV and V in Ga (up to 2109 mg kg^{-1}). Gallium rarely forms independent minerals, as söhngeite (Ga(OH)$_3$) and gallite (CuGaS$_2$) are the only naturally occurring crystalline high-content minerals that host Ga stoichiometrically (Yuan et al., 2021).

Gallium can be transported in near neutral pH fluids as Ga(OH)$_4^-$, which then precipitates with increasing temperature at constant pH as amorphous Ga(OH)$_3$. The latter can be adsorbed on minerals and aggregates of organic material. These aggregates can transport metals directly or serve as adsorption substrates for many trivalent and tetravalent ions, such as Ga, Ge, In, and Tl (Balistrieri et al., 2003; Pokrovski et al., 2002; Yuan et al., 2021). The strong affinity of Ga^{3+} for organic ligands, combined with the petrographic observations, would imply that organic material acted as an important ligand for the mobility of Ga (and Ge) at Djebel Gustar; especially because the sphalerite types associated with the former contain high concentrations of Ga (and Ge) (Wood and Samson, 2006). In addition, the presence of calcite (Sph IV) may also increase the amount of adsorbed Ga in solution and on adsorbing substrates (Pokrovsky et al., 2004). This may further suggest that hydrothermal calcitization might have played an important role in Ga-enrichment as evidenced by high Ga content in sphalerites associated with Qtz-Cal replacement veins (Sph IV) in contrast to ones deposited during dolomitizing event (Sph III and maybe Sph I and II).

Ga in its trivalent form is thought to enter the sphalerite crystal structure by a coupled substitution in combination with monovalent Cu (e.g., Ye et al., 2011). The correlation between Cu and Ga in the Djebel Gustar dataset suggests that Ga is incorporated into sphalerite through a coupled substitution mechanism (Ga^{3+} + Cu$^+$) → Zn^{2+}; Wei et al., 2018; Cugerone et al., 2021; Fig. 12a). The observation that Ga + Ge shows a better correlation with Cu than Ga alone (Fig. 12b), suggests that the recognized incorporation mechanisms are further complicated by the independent incorporation of other M^{2+}, M^{3+}, and M^{4+} cations. It is yet possible that Cu and Ga occur in sphalerite as nano-inclusions. Nano-inclusions of e.g. briartite (Cu$_2$(Zn,Fe)GeS$_4$) have been identified in Ge-rich sphalerite by atom probe tomography (Fougerouse et al., 2023). Hence it is possible that Cu-Ga phases are present in the Djebel Gustar sphalerite and are the reason for the elevated concentrations.

The trace elemental signature of sphalerite is a potentially important geothermometer (Möller, 1987; Bortnikov et al., 1995; Frenzel et al., 2016), however despite our best efforts we were unable to obtain a formation temperature from the Djebel Gustar deposits. We applied the Ga, Ge, In, Mn, and Ge in sphalerite thermometer of Frenzel et al. (2016) and obtained geologically unreasonable temperatures for the Djebel Gustar sphalerite (i.e., below the freezing point of water; see Appendix 1). This may be due to the geothermometer not being fully designed and calibrated for sphalerite with such high Ga and extremely low Fe concentrations as is the case of Djebel Gustar sphalerite. Additionally, we attempted to use fluid inclusion thermometry in sphalerite. Sphalerite types I and II were completely unsuitable for analysis due to their bleached and corroded textures. However, the observed inclusions are
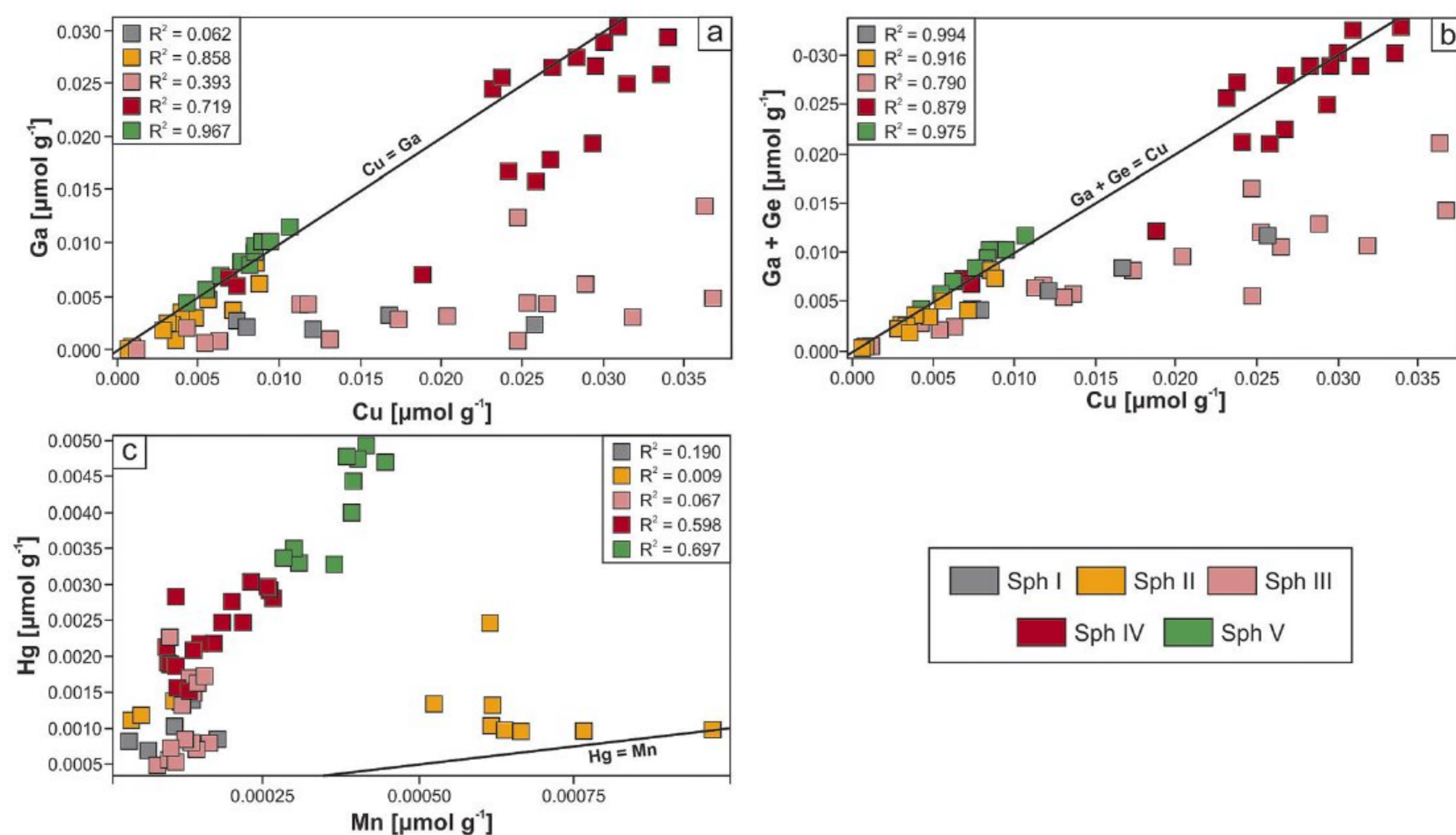

Fig. 12. Correlation plots of Cu vs. Ga, Cu vs. Ge, Pb vs. Sb and Mn vs. Hg concentrations in different sphalerite types for the total dataset for Djebel Gustar deposit.

mostly homogenous with a relatively small gaseous phase, which implies that they were most likely formed at temperatures below 300 °C (Roedder, 1984). The primary fluid inclusions found in sphalerite types III, IV, and V were all less than 10 μm, and therefore too small for a fluid inclusion study using our microscope. While we cannot determine a more exact depositional temperature of each sphalerite type, we can conclude that the previously suggested range of 120–240 °C is reasonable (Boutaleb, 2001; Lekbal and Boutaleb, 2012).

6.2. Trace element incorporation and photoluminescence

Sphalerite is a mineral known for its fluorescence when exposed to UV light (Saleh et al., 2019). Most commonly, sphalerite displays orange fluorescence under UV light, but other colors such as yellow, red, green, and blue can also occur. This fluorescence, however, can only occur in low-Fe varieties of sphalerite (<1.5 wt% Fe), since Fe acts as a fluorescence quencher (Götze, 2002; Çiftçi, 2009). The fluorescence color of sphalerite is mostly governed by the incorporation of small amounts of trace elements – activators. Incorporation of Mn^{2+} into sphalerite by produces orange fluorescence with a large band peaking at 595 nm (Boyle et al., 2007; Thi, 2009), while incorporation of Cl or Al into its crystal structure produces blue fluorescence with band peaks between 470 and 490 nm (Saleh et al., 2019). Complex coupled substitutions with combined monovalent and/or trivalent and tetravalent cations, such as $Cu^+ + Ga^{3+} \rightarrow 2Zn^{2+}$ have been shown to produce red fluorescence with band peaks between 640 and 675 nm (Goni and Rémond, 1969). Furthermore, Cu^+ itself has been proposed to be the cause for various emissions, including blue (at ~422 nm), red (at ~700 nm) and green (at ~520 nm) (Saleh et al., 2019 and references therein).

In the studied material from Djebel Gustar mine, five sphalerite types were identified, three of which produced fluorescence and one type that showed green phosphorescence (the afterglow after extinction of the long-wave UV light source) in addition to fluorescence (Fig. 6). The sphalerite type II displays orange fluorescence, which, due to its relatively high Mn content, could be attributed to its incorporation into the crystal structure of sphalerite by simple substitution $Mn^{2+} \rightarrow Zn^{2+}$ (e.g., Cao et al., 2018). The sphalerite type IV, which exhibits red luminescence, is characterized by a strong positive correlation between Cu and Ga. The red luminescence color observed has been explained by the presence of Cu^+ alone (Saleh et al., 2019), and the strong correlation between Cu/Ga makes it difficult for us to say whether this red color is indicative of Ga in sphalerite. The effects of Ga^{3+} on the photoluminescence of sphalerite has not yet been studied in detail, and it is feasible that it is an important co-activator or sensitizer to Cu (i.e., amplifies the effect of Cu). Sphalerites with red photoluminescence, due to Cu-Ga incorporation, have been reported in the Kipushi deposit of the Democratic Republic of Congo (Goni and Rémond, 1969), but again the strong link between Ga and Cu makes it difficult to separate the two in natural samples. Sphalerite type V is characterized by bright green luminescence and phosphorescence. Green emissions, and the phosphorescent response of artificial ZnS are well studied and widely utilized in several applications, for example in emergency signs in buildings, and is due to incorporation of Cu^+ into ZnS (Lisensky et al., 1996). The green photoluminescence could also occur due to randomly distributed donor–acceptor pair emission, with substitutional Cu^+ as an acceptor and a substitutional group IIIa or group VIIa element as donors (Saleh et al., 2019). As a group IIIa element, Ga^{3+} (median: 610 mg kg^{-1}) could be, in certain concentrations a suitable candidate to produce green photoluminescence in combination with Cu^+. However, that mechanism is not known to produce the bright green phosphorescence that was observed in Sph V (Saleh et al., 2019). The effects on photoluminescence of other trace elements present in high concentrations, such as Hg, Mn, and Cd remain unclear, as well the complex interplay of multiple elements (co-activators) occurring together in sphalerite.

7. Conclusions

The Djebel Gustar sphalerites occur in five types that can be distinguished based on their texture, mineral assemblage, and photoluminescence signature under longwave UV light. The differences in their general appearance, such as color and luminescence, can be reasonably correlated to their trace element content. The most important feature of the sphalerite from Djebel Gustar is the high concentration of critical elements such as Ga and Ge, but also elements that may pose an environmental risk (Hg, Cd). The strong correlation between Cu and Ga seem to indicate that coupled substitution is involved in the incorporation (i.e., $Cu^+ + Ga^{3+} \rightarrow 2Zn^{2+}$). Similarly, photoluminescence under UV light can be associated with trace element activators such as Mn^{2+} (orange), Cu^+ (red and green), and possibly Ga^{3+} (red), whereas Cu^+ is interpreted to be responsible for phosphorescence in one sphalerite type. The significant enrichment of the critical element Ga in Djebel Gustar is the result of the following conditions: Compared to sphalerite types I–III, we assume that the high Ga sphalerites (IV and V) were precipitated from a relatively Cl-poor hydrothermal fluid. This is also supported by the fact that Ga is not transported as a metal-chloride complex. The mineralizing fluids were also likely progressively reduced. Precipitation of Ga-rich sphalerites in Djebel Gustar is probably due to mixing of two fluids, one transporting mainly Zn and Pb (Cl-rich) and a reduced Cl-poor fluid containing considerable organic matter and calcite with adsorbed $Ga(OH)_3$ particles, that were subsequently incorporated in sphalerite.

Appendix A. Supplementary data

Supplementary data to this article can be found online at https://doi.

org/10.1016/j.oregeorev.2023.105474.

References

Balistrieri, L.S., Box, S.E., Tonkin, J.W., 2003. Modeling precipitation and sorption of elements during mixing of river water and porewater in the Coeur d'Alene River Basin. Environ. Sci. Tech. 37, 4694–4701. https://doi.org/10.1021/es0303283.

Bauer, M.E., Burisch, M., Ostendorf, J., Krause, J., Frenzel, M., Seifert, T., Gutzmer, J., 2019. Trace element geochemistry of sphalerite in contrasting hydrothermal fluid systems of the Freiberg district, Germany: insights from LA-ICP-MS analysis, near-infrared light microthermometry of sphalerite-hosted fluid inclusions, and sulfur isotope geochemistry. Miner. Deposita 54, 237–262. https://doi.org/10.1007/s00126-018-0850-0.

Belissont, R., Boiron, M.-C., Luais, B., Cathelineau, M., 2014. LA-ICP-MS analyses of minor and trace elements and bulk Ge isotopes in zoned Ge-rich sphalerites from the Noailhac – Saint-Salvy deposit (France): Insights into incorporation mechanisms and ore deposition processes. Geochim. Cosmochim. Acta 126, 518–540. https://doi.org/10.1016/j.gca.2013.10.052.

Bonnet, J., Mosser-Ruck, R., Caumon, M.-C., Rouer, O., Andre-Mayer, A.-S., Cauzid, J., Peifferet, C., 2016. Trace element distribution (Cu, Ga, Ge, Cd and Fe) in sphalerite from the Tennessee MVT deposits, USA, by combined EMPA, LA-ICP-MS, Raman spectroscopy, and crystallography. Can. Mineral. 54, 1261–1284. https://doi.org/10.3749/canmin.1500104.

Bortnikov, N.S., Dobrovol'skaya, M.G., Genkin, A.D., Naumov, V.B., Shapenko, V.V., 1995. Sphalerite-galena geothermometers; distribution of cadmium, manganese, and the fractionation of sulfur isotopes. Econ. Geol. 90 (1), 155–180. https://doi.org/10.2113/gsecongeo.90.1.155.

Bouabdellah, M., Sangster, D.F., 2016. Geology, Geochemistry, and Current Genetic Models for Major Mississippi Valley-Type Pb–Zn Deposits of Morocco. pp. 463–495. https://doi.org/10.1007/978-3-319-31733-5_19.

Boutaleb, A., Haddouche, A., Aïssa, D.E., Kolli, O., Sami, L., 2016. Metallogeny of carbonate hosted lead-zinc deposits in northeastern Algeria. In: 6th AARMC 1. pp. 1–5.

Boutaleb, A., Lekbal, F., 2012. Les minéralisations á Pb-Zn et barytine du Jurassique et de l'Aptiende la platforme Sétifienne (NE Algérien). In: Rabeau, O., Jébrak, M., Marquis, R. (Eds.), Programme et Résumés-Quatrièmes Journées De Launay. Ministère Des Ressources Naturelles et de La Faune, Québec, pp. 1–8.

Boutaleb, A. 2001. Les mineralisations a Pb-Zn du domaine Setifien-Hodna: Gitologie, petrographie, microthermometrie et implication metallogeniques. Doctoral Thesis. Universite des Sciences et de la Technologie H. Boumediene, Alger. 404 pp.

Boyle, T.J., Pratt, H.D., Hernandez-Sanchez, B.A., Lambert, T.N., Headley, T.J., 2007. Synthesis and optical properties of naturally occurring fluorescent mineral, ferroan sphalerite, inspired (Fe, Zn)S nanoparticles. J. Mater. Sci. 42 (8), 2792–2795. https://doi.org/10.1007/s10853-006-1419-3.

Burton, J.D., Culkin, F., Riley, J.P., 1959. The abundances of gallium and germanium in terrestrial materials. Geochim. Cosmochim. Acta 16 (1–3), 151–180. https://doi.org/10.1016/0016-7037(59)90052-3.

Cao, S., Zheng, J., Dai, C., Wang, L., Li, C., Yang, W., Shang, M., 2018. Doping concentration-dependent photoluminescence properties of Mn-doped Zn–In–S quantum dots. J. Mater. Sci. 53, 1286–1296. https://doi.org/10.1007/s10853-017-1598-0.

Cave, B., Perkins, W., Lilly, R., 2022. Linking uplift and mineralisation at the Mount Novit Zn-Pb-Ag Deposit, Northern Australia: Evidence from geology, U-Pb geochronology and sphalerite geochemistry. Geosci. Front. 13 (2), 101347 https://doi.org/10.1016/j.gsf.2021.101347.

Çiftçi, E., 2009. Mercurian sphalerite from Akoluk deposit (Ordu, NE Turkey): Hg as a cathodoluminescence activator. Mineral. Mag. 73, 257–267. https://doi.org/10.1180/minmag.2009.073.2.257.

Cook, N.J., Ciobanu, C.L., Pring, A., Skinner, W., Shimizu, M., Danyushevsky, L., Saini-Eidukat, B., Melcher, F., 2009. Trace and minor elements in sphalerite: A LA-ICPMS study. Geochim. Cosmochim. Acta 73, 4761–4791. https://doi.org/10.1016/j.gca.2009.05.045.

Cugerone, A., Cenki-Tok, B., Munoz, M., Kouzmanov, K., Oliot, E., Motto-Ros, V., Le Goff, E., 2021. Behavior of critical metals in metamorphosed Pb-Zn ore deposits: example from the Pyrenean Axial Zone. Miner. Deposita 56, 685–705. https://doi.org/10.1007/s00126-020-01000-9.

Decrée, S., Marignac, C., Abidi, R., Jemmali, N., Deloule, E., Souissi, F., 2016. Tectonomagmatic context of Sedex Pb–Zn and polymetallic ore deposits of the Nappe Zone Northern Tunisia, and comparisons with MVT deposits in the region. pp. 497–525. https://doi.org/10.1007/978-3-319-31733-5_20.

di Benedetto, F., Bernardini, G.P., Costagiola, P., Plant, D., Vaughan, D.J., 2005. Compositional zoning in sphalerite crystals. Am. Mineral. 90, 1384–1392. https://doi.org/10.2138/am.2005.1754.

European Commission, 2020. Critical Raw Materials Resilience: Charting a Path towards greater Security and Sustainability. https://eur-lex.europa.eu/legal-content/EN/TXT/PDF/?uri=CELEX:52020DC0474&from=EN.

Fougerouse, D., Cugerone, A., Reddy, S.M., Luo, K., Motto-Ros, V., 2023. Nanoscale distribution of Ge in Cu-rich sphalerite. Geochim. Cosmochim. Acta 346, 223–230. https://doi.org/10.1016/j.gca.2023.02.011.

Frenzel, M., Hirsch, T., Gutzmer, J., 2016. Gallium, germanium, indium, and other trace and minor elements in sphalerite as a function of deposit type — A meta-analysis. Ore Geol. Rev. 76, 52–78. https://doi.org/10.1016/j.oregeorev.2015.12.017.

George, L., Cook, N.J., Ciobanu, C.L., Wade, B.P., 2015. Trace and minor elements in galena: A reconnaissance LA-ICP-MS study. Am. Mineral. 100, 548–569. https://doi.org/10.2138/am-2015-4862.

George, L.L., Cook, N.J., Ciobanu, C.L., 2016. Partitioning of trace elements in co-crystallized sphalerite–galena–chalcopyrite hydrothermal ores. Ore Geol. Rev. 77, 97–116. https://doi.org/10.1016/j.oregeorev.2016.02.009.

Goni, J., Rémond, G., 1969. Localization and distribution of impurities in blende by cathodoluminescence. Mineral. Mag. 37, 153–155. https://doi.org/10.1180/minmag.1969.037.286.01.

Götze, J., 2002. Potential of cathodoluminescence (CL) microscopy and spectroscopy for the analysis of minerals and materials. Anal. Bioanal. Chem. 374, 703–708. https://doi.org/10.1007/s00216-002-1461-1.

Höll, R., Kling, M., Schroll, E., 2007. Metallogenesis of germanium—A review. Ore Geol. Rev. 30, 145–180. https://doi.org/10.1016/j.oregeorev.2005.07.034.

Hu, Y., Wei, C., Ye, L., Huang, Z., Danyushevsky, L., Wang, H., 2021. LA-ICP-MS sphalerite and galena trace element chemistry and mineralization-style fingerprinting for carbonate-hosted Pb-Zn deposits: Perspective from early Devonian Huodehong deposit in Yunnan, South China. Ore Geol. Rev. 136, 104253 https://doi.org/10.1016/j.oregeorev.2021.104253.

Kelley, K.D., Leach, D.L., Johnson, C.A., Clark, J.L., Fayek, M., Slack, J.F., Anderson, V. M., Ayuso, R.A., Ridley, W.I., 2004. Textural, compositional, and sulfur isotope variations of sulfide minerals in the red dog Zn-Pb-Ag deposits, Brooks Range, Alaska: Implications for ore formation. Econ. Geol. 99, 1509–1532. https://doi.org/10.2113/99.7.1509.

Laouar, R., Salmi-Laouar, S., Sami, L., Boyce, A.J., Kolli, O., Boutaleb, A., Fallick, A.E., 2016. Fluid inclusion and stable isotope studies of the Mesloula Pb-Zn-Ba ore deposit, NE Algeria: Characteristics and origin of the mineralizing fluids. J. Afr. Earth Sci. 121, 119–135. https://doi.org/10.1016/j.jafrearsci.2016.06.004.

Lee, J.H., Yoo, B.C., Yang, Y.-S., Lee, T.H., Seo, J.H., 2019. Sphalerite geochemistry of the Zn-Pb orebodies in the Taebaeksan metallogenic province, Korea. Ore Geol. Rev. 107, 1046–1067. https://doi.org/10.1016/j.oregeorev.2019.03.030.

Leikine, M., Vila, J.M., 1977a. Carte Géologique de l'Algérie 1: 50.000–Sheet Bir el Ahrech. Geological Survey of Algeria.

Leikine, M., Vila, J.M., 1977b. Carte Géologique de l'Algérie 1: 50.000–Sheet Mezloug. Geological Survey of Algeria.

Lekbal, F., Boutaleb, A., 2012. Les mineralisations Zn-Pb (Barytine) du Djebel Gustar (Sud Setifien), in: 2ème Colloque International Sur La Géologie Du Sahara: Ressources Minérales, En Hydrocarbures et En Eau. pp. 143–148.

Li, D., Tan, C., Miao, F., Liu, Q., Zhang, Y., Sun, X., 2019. Initiation of Zn-Pb mineralization in the Pingbao Pb-Zn skarn district, South China: Constraints from U-Pb dating of grossular-rich garnet. Ore Geol. Rev. 107, 587–599. https://doi.org/10.1016/j.oregeorev.2019.03.011.

Lisensky, G.C., Patel, M.N., Reich, M.L., 1996. Experiments with glow-in-the-dark toys: kinetics of doped ZnS phosphorescence. J. Chem. Educ. 75 (11), 1048. https://doi.org/10.1021/ed073p1048.

Liu, Q., Mei, Y., Etschmann, B., Glenn, M., MacRae, C.M., Spinks, S.C., Ryan, C.G., Brugger, J., Paterson, D.J., 2023. Germanium speciation in experimental and natural sphalerite: Implications for critical metal enrichment in hydrothermal Zn-Pb ores. Geochim. Cosmochim. Acta 342, 198–214. https://doi.org/10.1016/j.gca.2022.11.031.

Liu, S., Zhang, Y., Ai, G., Xue, X., Li, H., Shah, S.A., Wang, N., Chen, X., 2022. LA-ICP-MS trace element geochemistry of sphalerite: Metallogenic constraints on the Qingshuitang Pb-Zn deposit in the Qinhang Ore Belt, South China. Ore Geol. Rev. 141, 104659 https://doi.org/10.1016/j.oregeorev.2021.104659.

Luo, K., Cugerone, A., Zhou, M.F., Zhou, J.X., Sun, G.T., Xu, J., He, K.-J., Lu, M.D., 2022. Germanium enrichment in sphalerite with acicular and euhedral textures: an example from the Zhulingou carbonate-hosted Zn (-Ge) deposit, South China. Miner. Deposita 57 (8), 1343–1365. https://doi.org/10.1007/s00126-022-01112-4.

Martín-Martín, J.D., Vergés, J., Saura, E., Moragas, M., Messager, G., Baqués, V., Razin, P., Grélaud, C., Malaval, M., Joussiaume, R., Casciello, E., Cruz-Orosa, I., Hunt, D.W., 2017. Diapiric growth within an Early Jurassic rift basin: The Tazoult salt wall (central High Atlas, Morocco). Tectonics 36, 2–32. https://doi.org/10.1002/2016TC004300.

Möller, P., 1987. Correlation of homogenization temperatures of accessory minerals from sphalerite-bearing deposits and Ga/Ge model temperatures. Chem. Geol. 61, 153–159. https://doi.org/10.1016/0009-2541(87)90035-0.

Murakami, H., Ishihara, S., 2013. Trace elements of Indium-bearing sphalerite from tin-polymetallic deposits in Bolivia, China and Japan: A femto-second LA-ICPMS study. Ore Geol. Rev. 53, 223–243. https://doi.org/10.1016/j.oregeorev.2013.01.010.

Nassar, N.T., Graedel, T.E., Harper, E.M., 2015. By-product metals are technologically essential but have problematic supply. Sci. Adv. 1 (3), e1400180. https://doi.org/10.1126/sciadv.1400180.

Négrel, P., Ladenberger, A., Reimann, C., Birke, M., Sadeghi, M., 2018. Distribution of Rb, Ga and Cs in agricultural land soils at European continental scale (GEMAS): Implications for weathering conditions and provenance. Chem. Geol. 479 (20), 188–203. https://doi.org/10.1016/j.chemgeo.2018.01.009.

Omar, H., Abdelhak, B., Madjid, C., Saadia, Y., Hanafi, H., Djamel, B., 2016. Pb-Zn (Ba) deposits of the oriental Saharan Atlas (north-east of Algeria): distribution, control and implications for mining exploration. Arab. J. Geosci. 9, 422. https://doi.org/10.1007/s12517-016-2406-x.

Onuk, P., Melcher, F., Mertz-Kraus, R., Gäbler, H.-E., Goldmann, S., 2017. Development of a matrix-matched sphalerite reference material (MUL-ZnS-1) for calibration of in situ trace element measurements by laser ablation-inductively coupled plasma-mass spectrometry. Geostand. Geoanal. Res. 41, 263–272. https://doi.org/10.1111/ggr.12154.

Paton, C., Hellstrom, J., Paul, B., Woodhead, J., Hergt, J., 2011. Iolite: Freeware for the visualisation and processing of mass spectrometric data. J. Anal. At. Spectrom 26, 2508. https://doi.org/10.1039/c1ja10172b.

Pfaff, K., Koenig, A., Wenzel, T., Ridley, I., Hildebrandt, L.H., Leach, D.L., Markl, G., 2011. Trace and minor element variations and sulfur isotopes in crystalline and colloform ZnS: Incorporation mechanisms and implications for their genesis. Chem. Geol. 286 (3–4), 118–134. https://doi.org/10.1016/j.chemgeo.2011.04.018.

Pokrovski, G.S., Schott, J., Hazemann, J.-L., Farges, F., Pokrovsky, O.S., 2002. An X-ray absorption fine structure and nuclear magnetic resonance spectroscopy study of gallium–silica complexes in aqueous solution. Geochim. Cosmochim. Acta 66, 4203–4222. https://doi.org/10.1016/S0016-7037(02)00973-0.

Pokrovsky, O.S., Pokrovski, G.S., Schott, J., 2004. Gallium(III) adsorption on carbonates and oxides: X-ray absorption fine structure spectroscopy study and surface complexation modeling. J. Colloid Interface Sci. 279 (2), 314–325. https://doi.org/10.1016/j.jcis.2004.06.095.

Roberts, H., Price, R., Brombach, C.-C., Pichler, T., 2021. Mercury in the hydrothermal fluids and gases in Paleochori Bay, Milos, Greece. Marine Chem. 233, 103984 https://doi.org/10.1016/j.marchem.2021.103984.

Roedder, E., 1984. Fluid Inclusions. De Gruyter.

Rollinson, H.R., 1996. Using Geochemical Data. Longman & Harlow.

Saleh, M., Lynn, K.G., Jacobsohn, L.G., McCloy, J.S., 2019. Luminescence of undoped commercial ZnS crystals: A critical review and new evidence on the role of impurities using photoluminescence and electrical transient spectroscopy. J. Appl. Phys. 125 (7) https://doi.org/10.1063/1.5084738.

Sotillo, B., Fernández, P., Piqueras, J., 2015. Optical characterization of Ga-doped ZnS micro- and nanostructures. J. Mater. Sci. 50, 2103–2112. https://doi.org/10.1007/s10853-014-8772-4.

Thi, T.M., 2009. Influence of Mn2+ concentration and UV irradiation time on the luminescence properties of Mn-doped ZnS nanocrystals. Commun. Phys. 19 (1), 33–38. https://doi.org/10.15625/0868-3166/19/1/236.

USGS, (2020) Mineral Commodity Summaries: https://www.usgs.gov/centers/nmic/mineral-commodity-summaries.

Van Hinsbergen, D.J.J., Vissers, R.L.M., Spakman, W., 2014. Origin and consequences of western Mediterranean subduction, rollback, and slab segmentation. Tectonics 33, 393–419. https://doi.org/10.1002/2013TC003349.

Vaughan, D.J., Craig, J.R., 1997. Sulfide mineral stabilities, morphologies, and intergrowth textures. In: Barnes, H.L. (Ed.), Geochemistry of Hydrothermal Ore Deposits. John Wiley, New York, pp. 367–434.

Wei, C., Huang, Z., Yan, Z., Hu, Y., Ye, L., 2018. Trace element contents in sphalerite from the nayongzhi Zn-Pb deposit, northwestern Guizhou, China: Insights into incorporation mechanisms, metallogenic temperature and ore genesis. Minerals 8 (11), 490.

Wildi, W., 1983. La chaîne tello-rifaine (Algérie – Maroc - Tunisie): Structure, stratigraphie et evolution du Trias au Miocène. Rev. de géol. dynam. et de géogra. Physique 24, 201–297.

Wilson, S.A., Ridley, W.I., Koenig, A.E., 2002. Development of sulfide calibration standards for the laser ablation inductively-coupled plasma mass spectrometry technique. J. Anal. At. Spectrom. 17, 406–409. https://doi.org/10.1039/b108787h.

Wood, S.A., Samson, I.M., 2006. The aqueous geochemistry of gallium, germanium, indium and scandium. Ore Geol. Rev. 26 (1), 57–102. https://doi.org/10.1016/j.oregeorev.2003.06.002.

Xing, B.o., Mao, J., Xiao, X., Liu, H., Jia, F., Wang, S., Huang, W., Li, H., 2021. Genetic discrimination of the Dingjiashan Pb-Zn deposit, SE China, based on sphalerite chemistry. Ore Geol. Rev. 135, 104212.

Ye, L., Cook, N.J., Ciobanu, C.L., Yuping, L., Qian, Z., Tiegeng, L., Wei, G., Yulong, Y., Danyushevskiy, L., 2011. Trace and minor elements in sphalerite from base metal deposits in South China: A LA-ICPMS study. Ore Geol. Rev. 39, 188–217. https://doi.org/10.1016/j.oregeorev.2011.03.001.

Ysbaa, S., Haddouche, O., Boutaleb, A., Sami, L., Kolli, O., 2021. Mineralization and fluid inclusion characteristics of Pb-Zn-Fe-Ba (Cu, F, Sr) ore-deposits in northern east of Algeria. https://doi.org/10.1007/s12517-021-07281-2/Published.

Youcef Brahim, Mohammed, C., El-Hadi, M., Ramdane, M., Rami, D., Younes, M.C., Khoudir, K., 2021. Tectono-sedimentary evolution of eastern Algerian alpine foreland during Middle to Late Jurassic. Arab. J. Geosci. 14 (23) https://doi.org/10.1007/s12517-021-08806-5.

Yuan, W., Chen, J., Teng, H., Chetelat, B., Cai, H., Liu, J., Wang, Z., Bouchez, J., Moynier, F., Gaillardet, J., Schott, J., Liu, C., 2021. A review on the elemental and isotopic geochemistry of gallium. Glob. Biogeochem. Cycles 35 (9). https://doi.org/10.1029/2021GB007033.

Yuan, B., Zhang, C., Yu, H., Yang, Y., Zhao, Y., Zhu, C., Ding, Q., Zhou, Y., Yang, J., Xu, Y., 2018. Element enrichment characteristics: Insights from element geochemistry of sphalerite in Daliangzi Pb–Zn deposit, Sichuan, Southwest China. J. Geochem. Explor. 186, 187–201. https://doi.org/10.1016/j.gexplo.2017.12.014.

Zahri, F., Boukelloul, M.L., Hadji, R., Talhi, K., 2016. Slope stability analysis in open pit mines of Jebel Gustar career, NE Algeria – A multi-steps approach. Min. Sci. 137–146.

Zhong, R., Brugger, J., Chen, Y., Li, W., 2015. Contrasting regimes of Cu, Zn and Pb transport in ore-forming hydrothermal fluids. Chem. Geol. 395, 154–164. https://doi.org/10.1016/j.chemgeo.2014.12.008.

Zhuang, L., Song, Y., Liu, Y., Fard, M., Hou, Z., 2019. Major and trace elements and sulfur isotopes in two stages of sphalerite from the world-class Angouran Zn–Pb deposit, Iran: Implications for mineralization conditions and type. Ore Geol. Rev. 109, 184–200. https://doi.org/10.1016/j.oregeorev.2019.04.009.